Green Chemistry

PAPER

View Article Online
View Journal | View Issue

Cite this: *Green Chem.*, 2024, **26**, 7384

Advancing sustainable lignin valorisation: utilizing Z-scheme photocatalysts for efficient hydrogenolysis of lignin's β-O-4, α-O-4, and 4-O-5 linkages under ambient conditions†

Rajat Ghalta and Rajendra Srivastava *

Lignin, a crucial component of lignocellulosic biomass, holds immense promise for advancing biorefineries and producing sustainable energy alternatives. This study engineered a CN/rGO/BMO (2 : 1) heterojunction photocatalyst with varying Pd NP loading to selectively target the hydrogenolysis of challenging C–O ether bonds in lignin model compounds. Specific focus was on β-O-4, α-O-4, and the formidable 4-O-5 linkages. The 4-O-5 linkage, due to its high dissociation energy, poses a significant challenge. Electrochemical and spectral analyses unveiled improvements in charge separation, leading to delayed recombination of charge carriers in the heterojunction photocatalyst. Decorating the heterojunction with Pd NPs exhibited an elevated work function and a low Fermi energy level, facilitating the accommodation of photogenerated electrons and enabling efficient H_2 dissociation. Such enhancement facilitated the cleavage of all three linkages, including the resistant 4-O-5 bonds under ambient conditions. The photocatalyst exhibited effective cleavage, yielding aromatic (toluene, phenol, ethylbenzene) and aliphatic (cyclohexane, ethylcyclohexane) products. Selectivity modulation was achieved by adjusting the time, hydrogen pressure, and Pd loading. Furthermore, this photocatalytic approach successfully transformed simulated lignin bio-oil containing all three linkages into valuable monomers. The alcoholic solvents efficiently harnessed photogenerated holes and prevented electron–hole recombination. The photocatalyst also demonstrated the capability to produce monomers from the native lignin extracted from teak wood sawdust. Emphasizing the focus on the reaction pathway and mechanism, scavenging studies and analyses were conducted, including UPS and VBXPS, to establish the Z-scheme charge transfer mechanism within the heterojunction. These findings provide a sustainable and efficient pathway for lignin valorisation in biorefineries, significantly contributing to the advancement of green fuels and aligning with the principles of green chemistry.

Received 22nd February 2024,
Accepted 23rd April 2024

DOI: 10.1039/d4gc00898g

rsc.li/greenchem

Introduction

Lignin, a constituent of lignocellulosic biomass, holds immense promise in the future of biorefineries.[1] With its abundant energy content, accounting for a significant 40% of biomass energy, lignin has the potential to revolutionize the production of aromatic compounds and liquid fuels, offering a sustainable alternative to fossil fuels.[2] Composed mainly of phenylpropane units, such as *p*-coumaryl, coniferyl, and sinapyl alcohol, lignin is intricately interconnected through C–O and C–C bridge bonds.[3] Among these connections, the C–O ether bond, including β-O-4, α-O-4, and 4-O-5 linkages, plays a dominant role (Scheme 1a).[4,5]

To harness lignin efficiently, it becomes crucial to selectively cleave these aromatic ether bonds under mild conditions, preventing excessive hydrogenation of aromatic rings.[6–8] Traditional methods often rely on harsh chemicals

Catalysis Research Laboratory, Department of Chemistry, Indian Institute of Technology Ropar, Rupnagar, Punjab 140001, India. E-mail: rajendra@iitrpr.ac.in; Tel: +91-1881-232064

†Electronic supplementary information (ESI) available: Comprehensive insights into various aspects, encompassing experimental procedures, detailed synthesis of photocatalysts, and specifics of photocatalytic experiments. Nitrogen (N_2) adsorption and desorption profiles, Tauc plots illustrating the band gap of all photocatalysts, band structure calculations, GC mass chromatograph results, apparent quantum yield (AQY) calculations, size distributions of Pd NPs, TGA plots, analyses of spectral response, scavenging studies, and determination of elemental composition through XPS and EDX. Additionally, LSV analysis both in light and in the dark, NBT test spectra, PL spectra of THA solution, a comparative activity table, possible mechanisms, native lignin photocatalysis data, and recyclability studies. See DOI: https://doi.org/10.1039/d4gc00898g

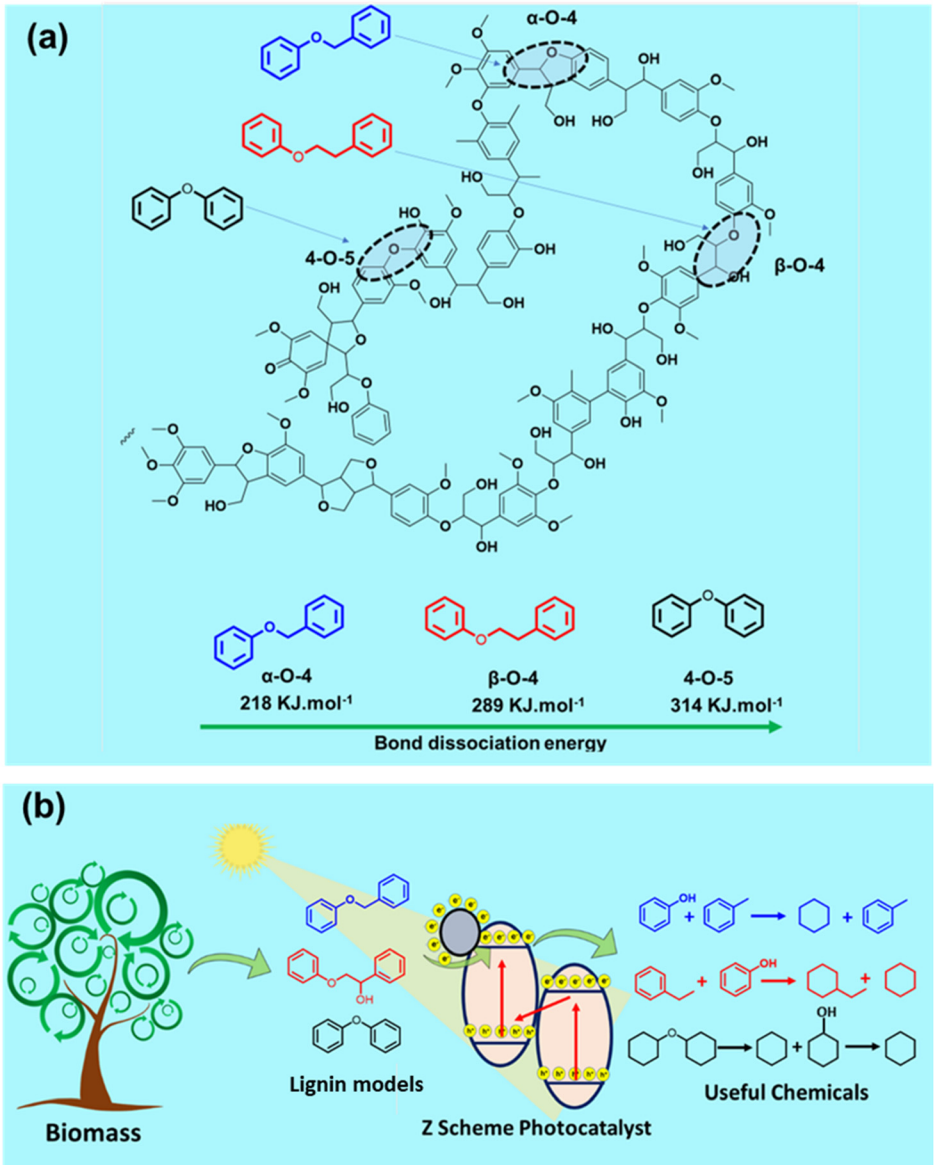

Scheme 1 (a) It illustrates the C–O linkages present in softwood lignin with varying binding energies, and (b) demonstrates the photocatalytic cleavage of all C–O linkages, followed by the valorisation of resulting fragments into aromatic and aliphatic monomers.

and excessive energy input, raising environmental concerns and limiting practicality.[9–11] This work presents a transformative approach that addresses these limitations, achieving selective transformation of all three C–O linkages (β-O-4, α-O-4, and 4-O-5) in lignin models and simulated bio-oil under mild conditions using visible light photocatalysis. Photocatalytic processes offer pathways for cleavage of C–O linkages through oxidative and reductive mechanisms.[12,13] In the reductive pathway, lignin model compounds undergo cleavage *via* hydrogenolysis.[14,15] While the cleavage of the α-O-4 linkage is relatively straightforward due to its lower dissociation energy, the photocatalytic cleavage of β-O-4 and 4-O-5 linkages presents challenges due to their higher dissociation energy (Scheme 1a).[5]

Ongoing research is focused on developing effective methods for the photocatalytic cleavage of these linkages.[12–14] Recent reports highlight promising advances in the photocatalytic cleavage of the β-O-4 linkage, leveraging sulphide-based photocatalysts such as $Zn_2In_2S_4$, $Zn_2Cd_2S_4$, CdS, and Ag@CdS.[16–24] In a notable study, a combination of Pd@$Zn_2In_2S_4$ and TiO_2 demonstrated the cleavage of the β-O-4 linkage, converting lignin model compounds into ketones and phenols, albeit with a dependence on UV light due to TiO_2.[25] Another study explored the use of different metals with CdS, revealing Ni/CdS as an effective catalyst for the photocatalytic cleavage of the β-O-4 linkage, albeit requiring the aid of 0.1 M KOH for full conversion.[20] With the limited exploration of α-O-4 bond cleavage in C–O configur-

ations, Han *et al.* synthesized the plasmonic Au-based 2.5Au-ASN-Ni^{2+} catalyst, achieving 98% conversion under visible light with equimolar toluene and phenol.[26] A limitation of this process is that it requires a base KOH as an additive. Liu *et al.* investigated α-O-4 bond cleavage using titanium nitride nanoparticles, achieving an 11% conversion rate under visible light at 100 °C.[27] However, this process has limitations due to the low conversion rate and the need for high temperatures. To date, there exists a solitary report on the cleavage of 4-O-5 linkages *via* the photocatalytic pathway employing 4%Pt(P25)@TiO_2, which necessitates the assistance of the strong acid HCl (1.2 equivalent) for the reaction and is exclusively active under UV light.[28] To our knowledge, no report explores all three linkages within a singular photocatalytic system.

After observing these gaps, such as the usage of acid–base additives, high-temperature requirement, utilizing UV light, and limited exploration of other linkages like α-O-4 and 4-O-5 in previous studies, we plan to develop a photocatalytic system that can successfully cleave all three C–O cleavages under mild conditions without any additives (Scheme 1b). It will be the first study showing that all the C–O linkages in lignin are cleaved through a single photocatalytic system, enhancing its practical applicability.

To achieve this endeavor, a Pd-loaded Z-scheme photocatalyst (Pd@CN/rGO/BMO) was strategically designed. The innovative design features a synergistic heterojunction between g-C_3N_4 (CN) and Bi_2MoO_6 (BMO), significantly enhancing charge separation and photocatalytic activity. Furthermore, reduced graphene oxide (rGO) facilitates efficient charge migration, and Pd nanoparticles (NPs) act as electron acceptors, further boosting the overall performance. The sustainable approach eliminates the need for harsh chemicals or excessive energy input, minimizing environmental impact and aligning with multiple principles of green chemistry. In this work, isopropanol (IPA) was employed, which is known for its low toxicity and environmental impact.[29] Furthermore, using visible light as the energy source minimizes energy consumption and reduces the carbon footprint associated with conventional energy sources.[30]

The photocatalytic system demonstrates exceptional performance, achieving 100% conversion of model compounds with high selectivity towards valuable aromatic products (toluene, phenol, ethylbenzene) and ring-reduced aliphatic compounds (cyclohexane, ethyl cyclohexane) under mild conditions. Interestingly, product selectivity can be manipulated by adjusting reaction parameters, offering tailored products for diverse applications. This flexibility expands the potential of lignin valorisation beyond traditional methods. The system was successfully tested with simulated bio-oils containing all three C–O linkages, achieving significant conversion to both aromatics and aliphatic. Furthermore, photocatalytic hydrogenolysis was conducted for lignin extracted from teak wood sawdust, highlighting its practical applicability for lignin valorization.

Experimental section

Catalyst synthesis

First, CN and BMO were synthesized using the previously reported methods.[31,32] A crucible containing 16 g of urea was taken and covered with a lid. It was heated in a muffle furnace at 550 °C for 3 h (Fig. 1). This annealing process resulted in the formation of CN, which was yellow in colour. The resultant material was subsequently finely ground into a powdered form. A solvothermal method was employed for the synthesis of BMO. A solution was prepared by dissolving 1.68 g of $Bi(NO_3)_3{\cdot}5H_2O$ and 0.421 g of $Na_2MoO_4{\cdot}2H_2O$ in 5 mL of ethylene glycol (Fig. 1). The solution was combined with 20 ml of ethanol and subjected to a solvothermal reaction in an autoclave, maintaining a temperature of 160 °C for 20 h. The resulting solid product, BMO, was separated, washed, and dried. To prepare Pd NPs supported CN, the CN powder was dispersed in ethanol, and a specific quantity of $PdCl_2$ and ethanol solution was added (Fig. 1). The resulting mixture was subjected to evaporation, followed by a reduction in a tube furnace at a temperature of 300 °C for 3 h under an H_2/Ar atmosphere to form Pd@CN. Furthermore, the experimental procedure involved mixing BMO with ethanol, Pd@CN, and graphene oxide (GO), followed by sonication for 4 h. The resulting mixture was then subjected to a solvothermal treatment at 120 °C for 8 h to form a composite material. The solvent was evaporated, and the resulting material was washed, resulting in the formation of a composite denoted as x%Pd@CN/rGO/BMO(y : 1), where x represents the weight percentage of Pd and y represents the composition ratio of the heterojunction. The details of photocatalyst synthesis, with complete protocols and the amounts of precursors and reagents used, are provided in the ESI.†

Catalytic reaction

The photocatalytic hydrogenolysis of various lignin models was carried out by introducing the necessary reactant, photocatalyst, and solvent into a glass reactor pressurized with hydrogen gas. The reaction mixture was irradiated with either a 150 W white LED or sunlight, with constant stirring for a specified duration. Illustrations of the photocatalytic reactor setup can be referenced in Fig. S1 and S2.† Post-reaction, the photocatalyst was isolated through centrifugation, resulting in a transparent reaction mixture. The progression of the reaction was tracked using gas-chromatography (GC), while gas-chromatography-mass spectrometry (GC-MS) was utilized for product identification (Fig. S3–S9†). The apparent quantum yield (AQY) was determined using a well-established method. Comprehensive details about the photocatalytic reaction specifics, reactor setup, lignin extraction, photocatalytic reactor setup for extracted lignin, quantification of reaction activity, and the AQY calculation are available in the ESI.† Furthermore, the ESI† provides in-depth information on the nitroblue-tetrazolium (NBT) and terephthalic-acid (THA) tests.

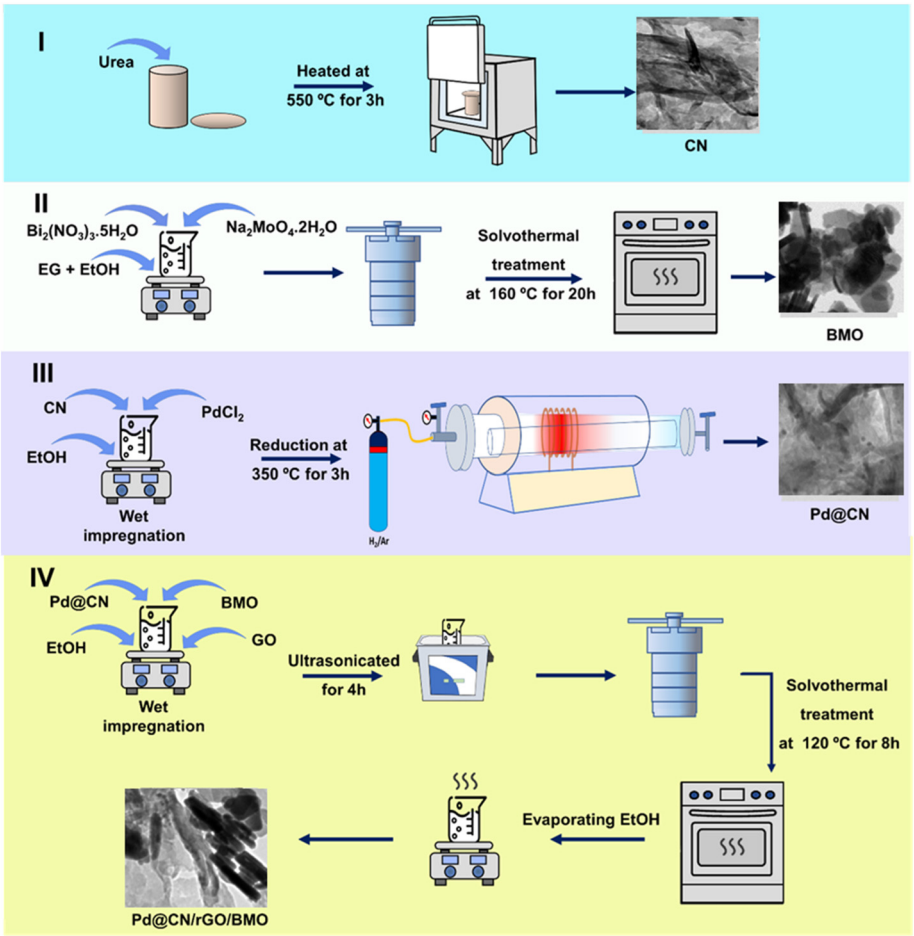

Fig. 1 Schematic presentation (I to IV) of the experimental process for the synthesis of Pd@CN/rGO/BMO.

Results and discussion

Physicochemical characterization

X-ray diffraction (XRD) analysis provided detailed structural insights into pristine components (CN, GO, BMO) and their composite variations. The analysis of pristine CN revealed a layered graphitic arrangement with a distinct (002) plane peak at 27.41° (Fig. 2a), indicating its ordered structure.[33] Further insights into the layer steaking came from the observed (100) diffraction plane peak at 13.1°. For GO, prepared *via* an enhanced Hummers' method, a dominant peak at 11.2° (2θ) corresponded to its (002) planes (Fig. 2a).[34] Additionally, the XRD pattern of BMO matched well with the JCPDS card no. 76-2388, exhibiting peaks at various 2θ values (*e.g.*, 10.97°, 23.6°, 28.21°) confirming its orthorhombic phase (Fig. 2a).[31] In the XRD patterns of x%Pd@CN/rGO/BMO(1 : y) nanocomposites, the CN peak at 27.41° either disappeared or overlapped with the BMO's (111) peak, while the BMO-related peaks remained prominent due to its higher crystallinity (Fig. 2b).[35] Notably, decreasing BMO content in the composite further attenuated its corresponding peaks (Fig. 2b). The introduction of Pd NPs resulted in a new peak at 40.3°, assigned to the Pd NPs (111) plane (Fig. 2b).[36] Furthermore, higher Pd loading led to a stronger signal for this peak, confirming the successful integration of Pd NPs on the photocatalyst (Fig. 2c).

As the peaks corresponding to CN in the XRD pattern of CN/rGO/BMO(1 : y) are obscured by the intense peaks of BMO due to the high crystallinity of BMO, necessitating additional analysis to confirm CN's presence in the nanocomposite. The FT-IR spectrum of CN exhibits a broad band between 3000 cm^{-1} and 3450 cm^{-1}, encompassing N–H and O–H stretching vibrations from surface oxygen, along with a sharp peak at 810 cm^{-1} corresponding to the heptazine ring system (Fig. S10†).[32,37] These peaks are present in the composite material, with their intensity increasing proportionally to the CN content (Fig. S10b and c†). Additionally, weak peaks between 400 cm^{-1} and 850 cm^{-1}, assigned to Bi–O, Mo–O, and Mo–O–Mo stretching modes, confirm the presence of BMO and CN in the composite.[38] The absence of FT-IR peaks from rGO signifies its minimal contribution to the composite due to its low concentration.

FE-SEM analysis revealed the intricate microstructure of the components. Unmodified BMO displayed a flower-like morphology with interlaced nanosheets spanning micrometers

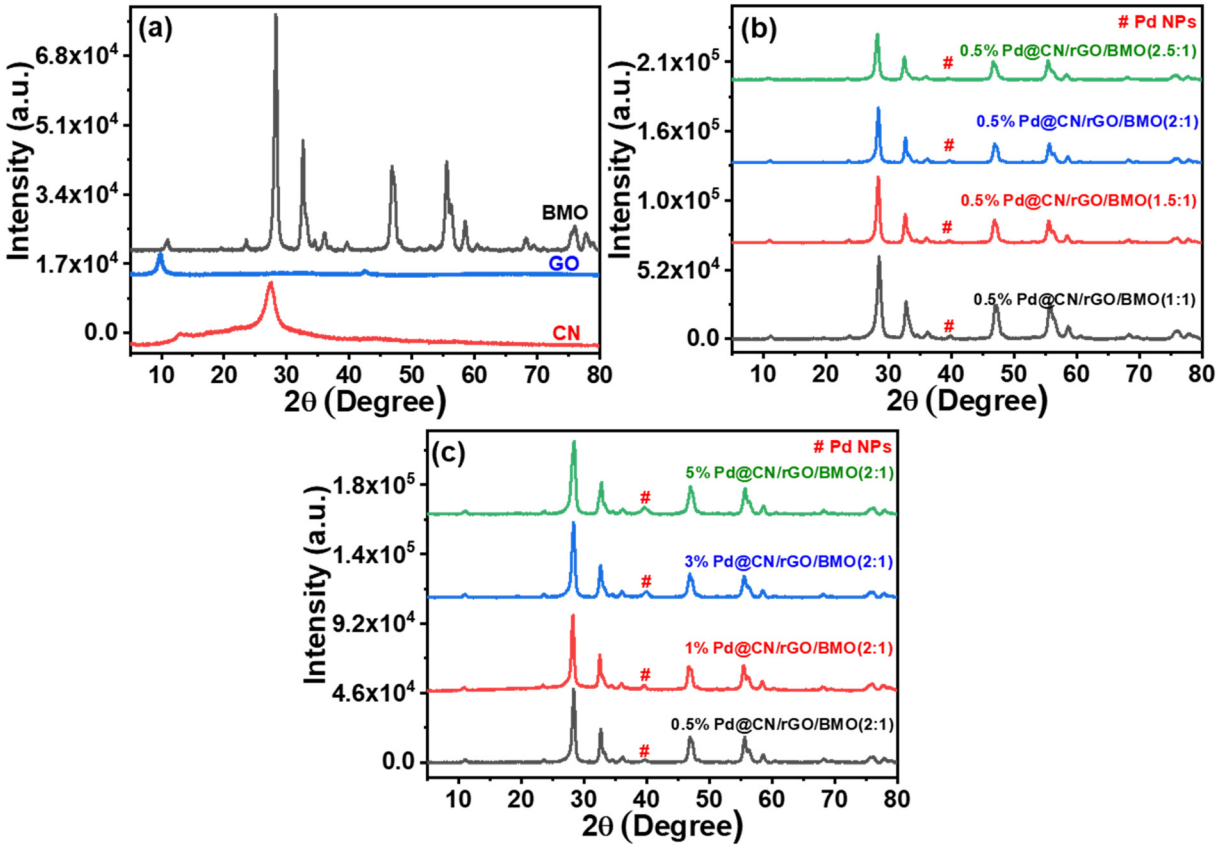

Fig. 2 XRD patterns of (a) CN, GO and BMO, (b) different composites with 0.5% Pd loading, and (c) *x*% Pd@CN/rGO/BMO(2 : 1) heterojunction with different Pd loadings.

(Fig. 3a and S11a, b†).[31] CN exhibited a sheet-like structure (Fig. 3b and S11c, d†), while GO presented a densely steaked, layer-by-layer arrangement (Fig. 3c and S11e†).[39] The CN/rGO/BMO(2 : 1) composite show distinct features. BMO nanosheets extended over CN sheets, forming a 3D hierarchical structure (Fig. 3d, e and S11f, g†). It highlights a steaked and interconnected network at their interface. Notably, GO sheets were scarce due to their low concentration. HR-TEM corroborated these observations (Fig. 3f–h). For 3%Pd@CN/rGO/BMO(2 : 1), HR-TEM revealed BMO nanosheets over the larger CN sheets (Fig. 3i), with lattice fringes indicating the (131) and (200) planes of BMO (Fig. 3j).[31,40] Well-dispersed Pd NPs were observed over the surface (Fig. 3j and k). Remote lattice fringes corresponded to the (111) plane of Pd NPs (Fig. 3l).[36,41] HR-TEM images were utilized to calculate the particle size of Pd NPs from the distribution histogram (Fig. S12†), which was 5.2 nm. Energy-dispersive X-ray (EDX) analysis confirmed the elemental composition of 3%Pd@CN/rGO/BMO(2 : 1), detecting carbon (C), bismuth (Bi), nitrogen (N), molybdenum (Mo), oxygen (O), and palladium (Pd) (Fig. 3m–r) (Table S1†). Microwave-plasma atomic-emission spectroscopy (MPAES) measured the bulk weight present of Pd in 0.5%, 1%, 3%, and 5% Pd@CN/rGO/BMO(2 : 1) catalysts, showing 0.46%, 0.92%, 2.85%, and 4.69%, respectively.

Thermal stability analysis revealed significant differences between the individual components and the composite materials. BMO displayed remarkable resistance, losing only 9% of its weight up to 750 °C (Fig. S13†). In contrast, CN completely degraded at the same temperature (Fig. S13†). It highlights the stabilizing effect of BMO within the composite heterojunction, which exhibits only partial degradation. 3% Pd@CN/rGO/BMO(2 : 1) led to slightly higher residue than the CN/rGO/BMO(2 : 1) composite at 750 °C, confirming Pd's presence. Moreover, all catalysts remained thermally stable up to 430 °C, indicating their resistance to decomposition at high temperatures. Insights into the textural properties were derived from BET analysis (Fig. S14†). CN/rGO/BMO(2 : 1) and its Pd-decorated sample exhibited type II adsorption, indicating interparticle porosity within the nanocomposites.[37] Furthermore, the integration of BMO into the CN matrix prominently augmented the surface area, escalating it from 24 $m^2\ g^{-1}$ (for bare BMO) to 38 $m^2\ g^{-1}$ (for CN/rGO/BMO(2 : 1)). The presence of metallic components had a minimal impact on the surface area of the composite, likely due to the additional N_2 adsorption sites facilitated by the presence of Pd NPs.[42,43] The details of the surface area and total pore volume for the catalysts are comprehensively outlined in Table S2.†

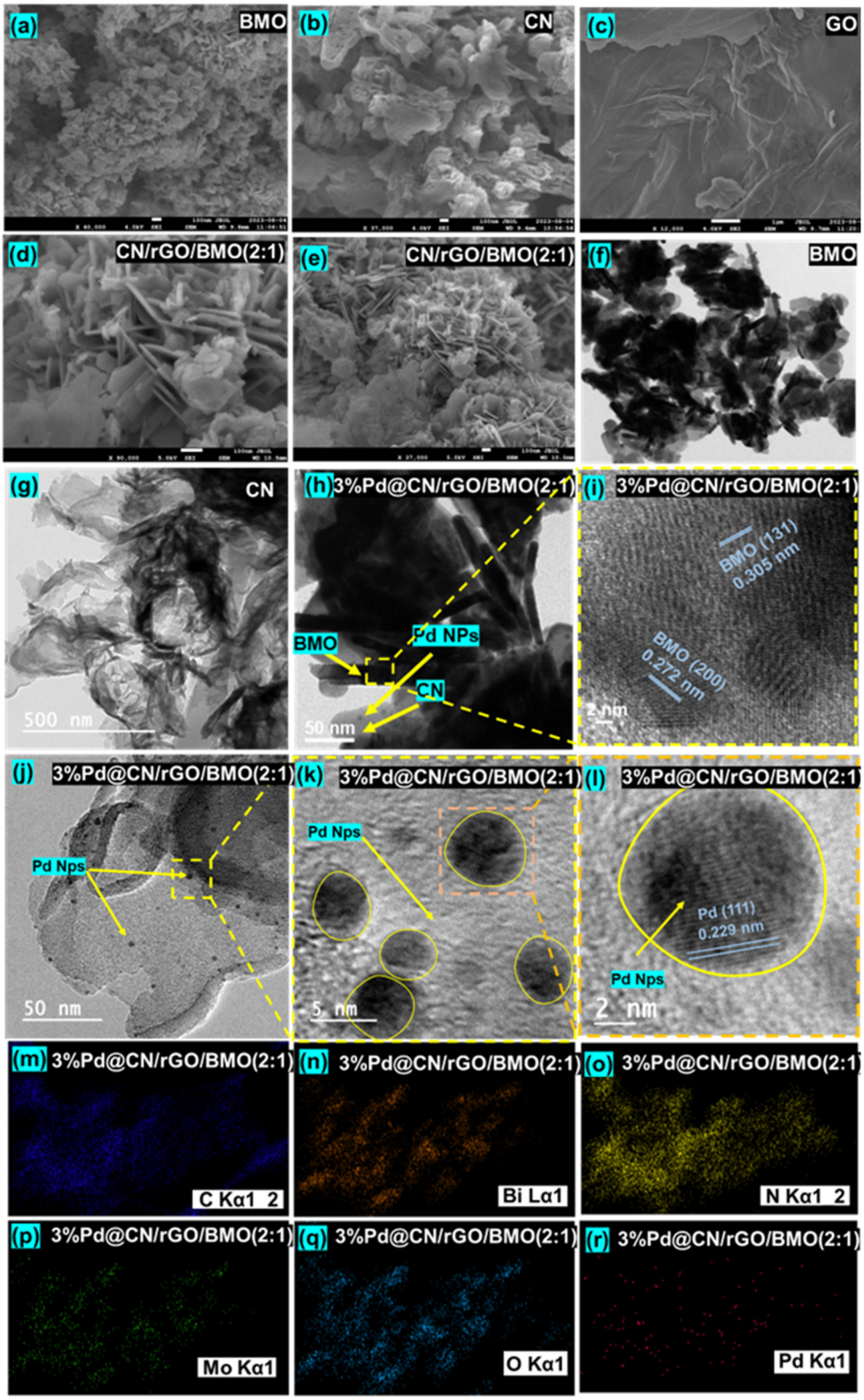

Fig. 3 FE-SEM (a) pristine BMO, (b) CN, (c) GO, and (d and e) CN/rGO/BMO(2 : 1) composite, HR-TEM images (f) BMO and (g) CN, (h–l) 3%Pd@CN/rGO/BMO(2 : 1) and (m–r) elemental mapping of 3%Pd@ CN/rGO/BMO(2 : 1).

X-ray photoelectron spectroscopy (XPS) provided the chemical states of constituent elements in the 3% Pd@CN/rGO/BMO (2 : 1) heterojunction, BMO, and CN photocatalysts. In the 3% Pd@CN/rGO/BMO(2 : 1) heterojunction, a surface survey (Fig. S15†) (Table S3†) was conducted to analyze the inclusion of Bi, Mo, O, C, N, and Pd. Specifically, elemental analysis revealed the composition of Bi, Mo, and O in BMO, while CN comprised C, N, and O in its structural matrix. In the XPS examination of 3% Pd@CN/rGO/BMO(2 : 1), the magnified spectrum of Bi 4f displayed distinct peaks at 159.07 eV (Bi $4f_{7/2}$) and 164.35 eV (Bi $4f_{5/2}$) (Fig. 4a), confirming the Bi^{3+} species.[44] Similar Bi peaks were observed in pristine BMO at 159.14 eV and 164.44 eV (Fig. 4a and g). Mo 3d peaks were identified at 235.50 eV (Mo $3d_{3/2}$) and 232.31 eV (Mo $3d_{5/2}$) in the 3% Pd@CN/rGO/BMO(2 : 1) spectra (Fig. 4b), indicating the Mo^{+6}, akin to the observed peaks in pristine BMO at 232.42 eV and 235.56 eV (Fig. 4b and h).[45] O 1s spectrum of 3% Pd@CN/rGO/BMO(2 : 1) unveiled four different peaks with binding energies of 529.95, 530.93, 532.43, and 533.85 eV, corresponding to various oxygen species, including Mo–O/Bi–O, surface –OH species in BMO, surface oxygen of CN, and oxygen in (O–N) intermediates of CN (Fig. 4c).[37,46] Correspondingly, pristine BMO and CN displayed different oxygen types, represented by distinct binding energies (Fig. 4i

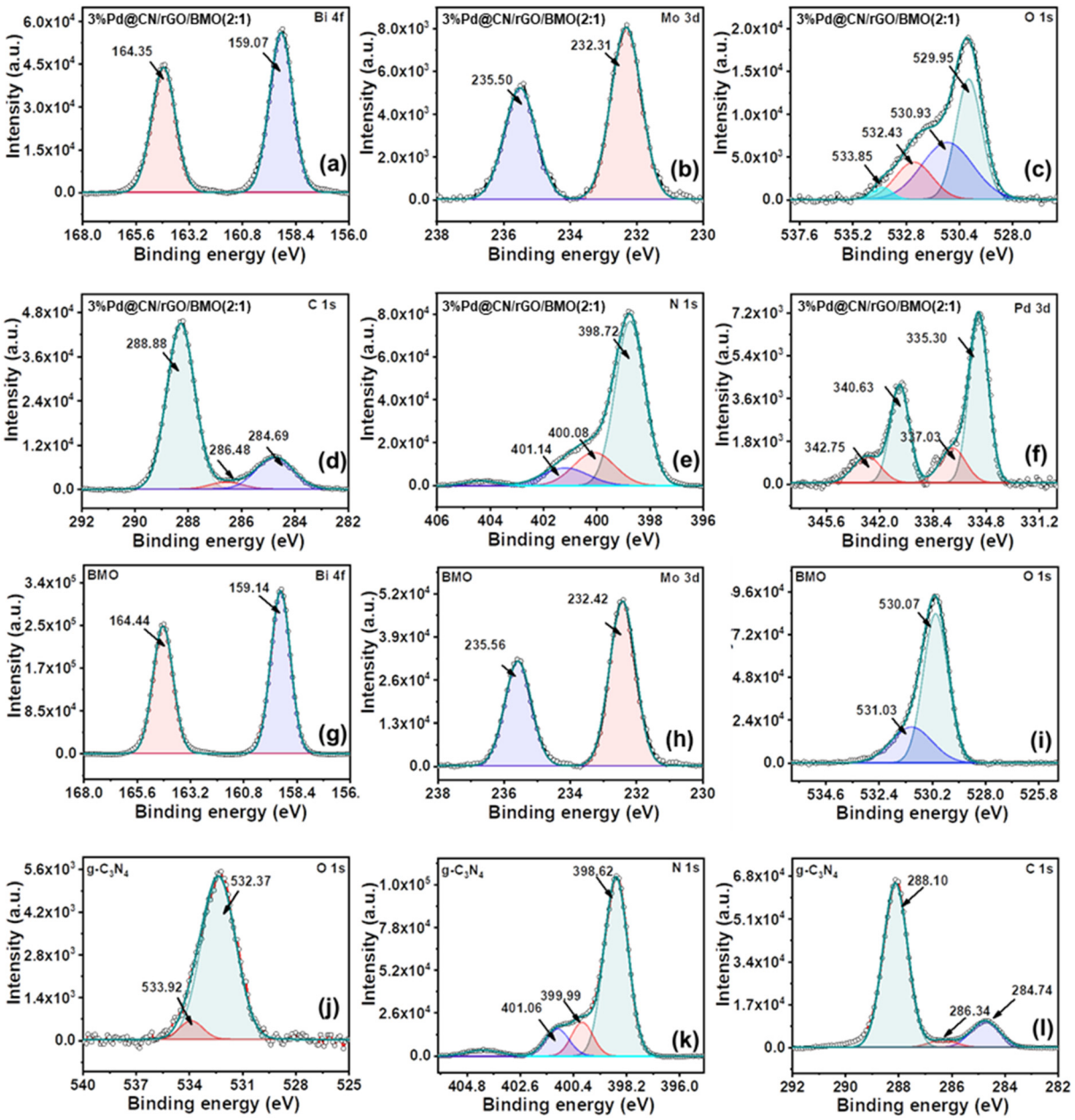

Fig. 4 Resolved XPS profiles of (a) Bi-(4f), (b) Mo-(3d), (c) O-(1s), (d) C-(1s), (e) N-(1s) and (f) Pd-(3d) for 3%Pd@CN/rGO/BMO(2 : 1); (g) Bi-(4f), (h) Mo-(3d) and (i) O-(1s) of BMO; and (j) O-(1s), (k) N-(1s), and (l) C-(1s) of CN.

and j). In the C 1s XPS analysis of 3% Pd@CN/rGO/BMO(2 : 1), three types of carbon are evident at different binding energies (Fig. 4d), similar to pristine CN (Fig. 4l).[32] Furthermore, the deconvoluted N 1s spectrum of 3% Pd@CN/rGO/BMO(2 : 1) exhibited three peaks at 398.72 eV (pyridinic N), 400.08 eV (NC_3), and 401.14 eV (NH_x amine functional groups) (Fig. 4e), aligning with the nitrogen species in pristine CN (Fig. 4k).[47] The deconvoluted XPS profile for Pd 3d in 3% Pd@CN/rGO/BMO(2 : 1) shows two peaks signifying the Pd $3d_{3/2}$ and Pd $3d_{5/2}$ states, indicating the spin orbit coupling phenomenon (Fig. 4f).[48] The peaks detected at binding energies 340.63 eV and 335.30 eV are attributed to Pd^0, while those with binding energies of 342.75 eV and 337.03 eV are associated with Pd^{2+}.[49] The analysis suggested that Pd atoms primarily existed in Pd NPs in a zero oxidation (Pd^0) state with a low concentration of Pd^{2+} (PdO).[36]

Optical properties

To evaluate the synergistic effects of BMO and CN, their optical properties and those of the synthesized heterojunctions were scrutinized with solid-state diffuse reflectance ultraviolet-visible spectroscopy (DRUV-vis) (Fig. 5a). The photocatalysts exhibited band gaps in the visible part of the spectrum, with CN displaying an absorption-edge in the visible-range bordering the UV part. The construction of the CN and BMO heterojunction revealed a noticeable increase in wavelength (red shift) in their absorbance spectra, often indicating structural modifications or material interactions. Bandgap assessments *via* Tauc plots (Fig. S16†) (Table S4†) allowed the estimation of the heterojunction's bandgap, falling within the range defined for BMO and CN bandgap values.[50–52] The comprehensive optical examination and bandgap analysis illuminate the combined impact of the two materials within the heterojunction, providing insight into the observed enhancement in photocatalytic activity (discussed below).

In the photoluminescence (PL) analysis, CN displayed strong emission throughout the visible spectrum, reaching a peak of 466 nm (Fig. 5b) under an excitation wavelength of 335 nm. BMO demonstrated a similar but comparatively broader emission. However, upon forming a CN/rGO/BMO (2 : 1) heterojunction, an observable enhancement in charge separation was witnessed, reducing the emission intensity.[53] The introduction of Pd decoration in the nanocomposites resulted in diminished and broader emission characteristics, ascribed to the excellent electron capture capability of Pd NPs, effectively facilitating charge separation and extending the lifetime of charge pairs by minimizing recombination events. Time-Correlated Single-Photon Counting (TCSPC) provided precise decay profiles (Fig. 5c).[54–56] The composite material exhibited a significantly longer average decay lifetime of 3.74 nanoseconds (ns) compared to the individual material (Table S5†). Pd incorporation further extended the lifetime to 4.17 ns, highlighting the nanocomposite's superior performance. The extended lifetime suggests efficient electron trapping and accommodation by Pd NPs, enhancing overall charge retention.

Photoelectrochemical analysis

The transient photocurrent was recorded *via* light on–off electrochemical experiments (Fig. 5d). Upon light irradiation, the catalysts exhibited an increased current response that rapidly reverted upon light cutoff, demonstrating stable and repetitive behavior across multiple cycles. A comparative assessment revealed BMO to exhibit a moderately higher response than CN, indicative of slower recombination for BMO, while CN displayed higher susceptibility to charge recombination. The CN/rGO/BMO(2 : 1) heterojunction demonstrated an improved response owing to enhanced charge carrier separation, further enhanced with an increased Pd content, observed in the 5%Pd@CN/rGO/BMO(2 : 1) catalyst due to its elevated conductivity. The catalyst exhibited a noticeable enhancement in charge carrier population and movements during light exposure, establishing enhanced activity *via* the relationship between carrier concentration (N) and electrical- conductivity (σ) specified as $\sigma = Ne\mu$.[57]

Linear sweep voltammetry (LSV) investigations were performed under dark and illuminated conditions (Fig. S17†) and displayed a noticeable increment in current density with increasing potential in both scenarios. The materials showed varied current densities at 1.7 V *versus* Ag/AgCl: CN (0.8×10^{-4} A cm^{-2}), BMO (1.5×10^{-4} A cm^{-2}), and CN/rGO/BMO(2 : 1) (2.7×10^{-4} A cm^{-2}) in the dark. Under light, these values escalated for CN (1.5×10^{-4} A cm^{-2}), BMO (2.4×10^{-4} A cm^{-2}), and CN/rGO/BMO(2 : 1) (4.2×10^{-4} A cm^{-2}), demonstrating light-induced activity.[37] The heterojunction photocatalysts exhibited improved charge carrier transport, which further enhanced upon incorporating Pd NPs, reaching the topmost current density value of 5.8×10^{-4} A cm^{-2} at 1.7 V *versus* Ag/AgCl upon light irradiation.

Electrochemical Impedance Spectroscopy (EIS) provided Nyquist plots (Fig. 5e), where the semicircular shape indicated interfacial charge migrations.[58] The semicircle diameter, directly linked to the interfacial charge-transfer resistance (R_{ct}) between the electrode and electrolyte, revealed varying R_{ct} values for CN, BMO, CN/rGO/BMO(2 : 1), and Pd-decorated CN/rGO/BMO(2 : 1) catalysts.[59,60] The observed trend reflected progressive enhancement in charge transfer properties from BMO to CN/rGO/BMO(2 : 1), and further increased upon Pd integration, emphasizing the material's increasingly efficient charge transfer process.

Band structure analysis

The Mott–Schottky (MS) electrochemical experiment results were utilized to analyze the band edges of CN and BMO (detailed calculations are available on page S14, ESI†).[61–64] E_{fb} values of CN and BMO were −1.13 and −0.26 V *vs.* Ag/AgCl (Fig. 5f). Additionally, the energy band edges were calculated using the E_{fb} values obtained from the MS experiment. The E_{CB} values for CN and BMO were −1.03 and −0.16 *vs.* NHE. Using the value of E_{CB} and band gap. The value of E_{vb} for CN and BMO was estimated to be 1.73 and 2.64 *vs.* NHE using relation $E_{VB} = E_{CB} + E_g$.

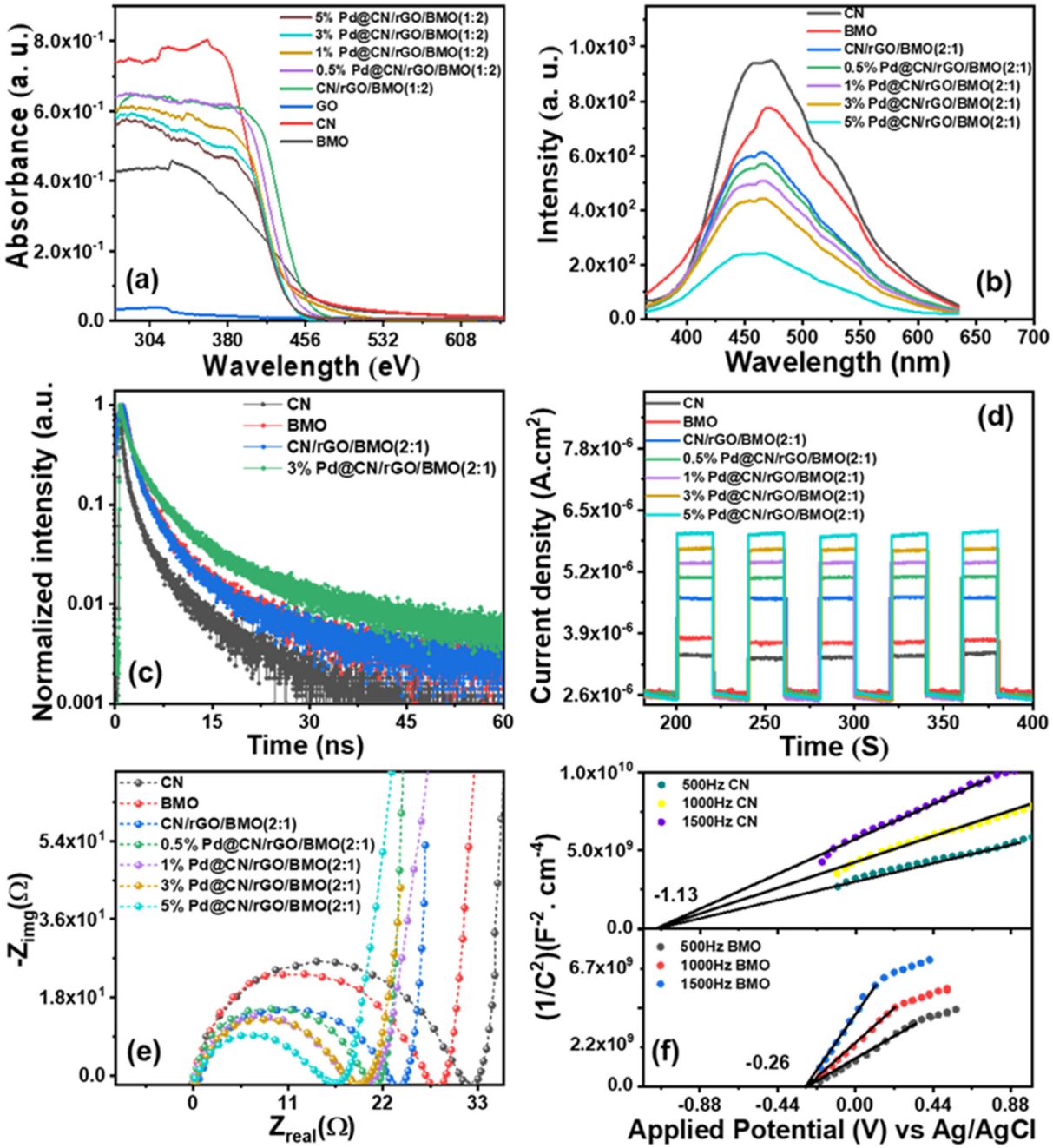

Fig. 5 (a) DRUV-vis spectra, (b) PL spectra, (c) TCSPC spectra, (d) on–off transient photocurrent , (e) EIS spectra and (f) M.S plots for different heterojunction based photocatalysts.

The comprehensive band architectures of CN, BMO, and the CN/rGO/BMO(2 : 1) composite were investigated employing valence-band X-ray photoelectron spectroscopy (VB-XPS), ultraviolet photoelectron spectroscopy (UPS), and solid-state diffuse reflectance ultraviolet-visible spectroscopy (DRUV-vis).[32,43] VB-XPS analysis revealed the valence band maxima (VBM) for CN and BMO at 1.55 eV and 2.04 eV, respectively, with reference to their corresponding Fermi levels (E_f) (Fig. 6a and c).[65] The Fermi levels in CN and BMO correspond to their work function (Φ), signifying the energy gap between the Fermi and vacuum levels (V_{ac}).[66] The Φ for CN and BMO, derived from UPS spectra, were calculated as 4.58 eV and 4.92 eV, using equation $\Phi = 21.22 - E_{SEcut\ off} + E_{cutoff}$ (Fig. 6b and d).[67] The integration of VB-XPS, DRUV-vis, and UPS techniques, determined the conduction and valence band positions for CN at 6.13 eV and 3.37 eV, *vs.* V_{ac} (Fig. 6e). For BMO, these values were 6.96 eV and 4.32 eV, respectively (Fig. 6e), initially calculated in E_{vac} and later transformed into E_{NHE} with equation, $E_{NHE} = E_{vac} - (4.44 \pm 0.02)$.[68] The alignment of band edges between CN and BMO, as projected by MS, was observed.[69]

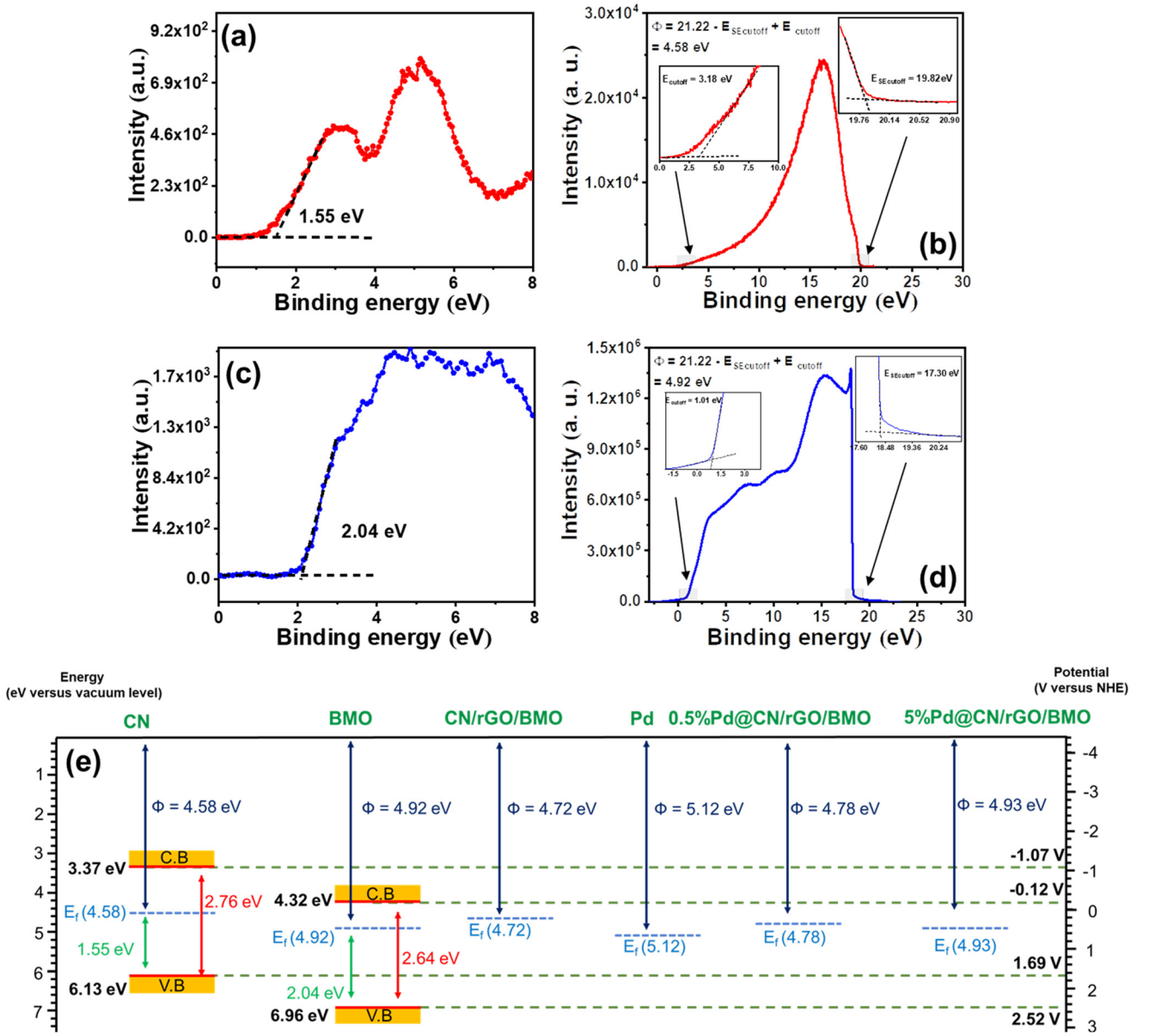

Fig. 6 (a) VB-XPS spectrum for CN, (b) UPS spectrum for CN, (c) VB-XPS spectrum for BMO, and (d) UPS spectrum for BMO and (e) (a)calculated band-structures for CN, BMO, CN/rGO/BMO(2 : 1), 0.5%Pd@CN/rGO/BMO(2 : 1), and 5%Pd@CN/rGO/BMO(2 : 1).

Upon integration into a heterojunction material, the Fermi level of CN (4.58 eV *vs.* V_{ac}) underwent a reduction, while BMO's Fermi level (4.92 eV *vs.* V_{ac}) increased. This resulted in a new equilibrium at 4.72 eV *vs.* V_{ac}, as obtained from the UPS analysis of CN/rGO/BMO(2 : 1) (Fig. S17a†).[69] It induced upward band bending in CN and downward band bending in band edges of BMO near the interface (refer to Fig. 10a(i) and (ii)).[43] Upon reaching equilibrium, the charge transmission pathway at the CN-BMO interface became non-reactive, disrupting the charge migration because of band bending. Consequently, the composite exhibited a discrete Fermi level at 4.72 eV *vs.* V_{ac}. Pd NPs have a reported Fermi level of 5.12 eV *vs.* V_{ac}.[70–72] Upon incorporating Pd NPs into the heterojunction, the Fermi level of the CN/rGO/BMO(2 : 1) composite aligned with the Fermi level of Pd NPs at 5.12 eV *vs.* V_{ac}.[69] It led to resifting of the Fermi level at 4.78 eV *vs.* V_{ac} for 0.5% Pd@CN/rGO/BMO(2 : 1) and 4.93 eV *vs.* V_{ac} for 5%CN/rGO/BMO(2 : 1) catalysts (Fig. S18b and c†). The higher work function (Φ) of Pd compared to CN/rGO/BMO(2 : 1) enables the facile transfer of photogenerated electrons from the heterojunction's conduction band (CB) to the Pd NPs (Fig. 9a(iv)).[43]

Photocatalytic activity

The study explores the photocatalytic hydrogenolysis of benzyl phenyl ether (BPE), a model compound mimicking the crucial α-O-4 linkage found in lignin, a promising renewable resource.

Utilizing a 0.5% Pd@CN, 2 bar hydrogen pressure, and irradiation from a 150 W LED at ambient temperature, the optimal photocatalyst loading for maximizing BPE conversion was studied, resulting in the identification of quantity (20 mg), and yielding a peak activity marked by 38.6% BPE conversion (Fig. 7a). Notably, the reaction displayed outstanding selectivity, producing nearly equimolar quantities of phenol (PhOH) and toluene (TOL) as the primary products, with negligible byproduct formation.

In pursuit of optimal illumination, experimentation with various light sources was undertaken. The 150 W LED, demonstrated efficient α-O-4 linkage cleavage, achieving 38.6% BPE conversion in 3 h, with TOL and PhOH as the predominant products (Fig. 7b). Exposure to sunlight yielded the highest

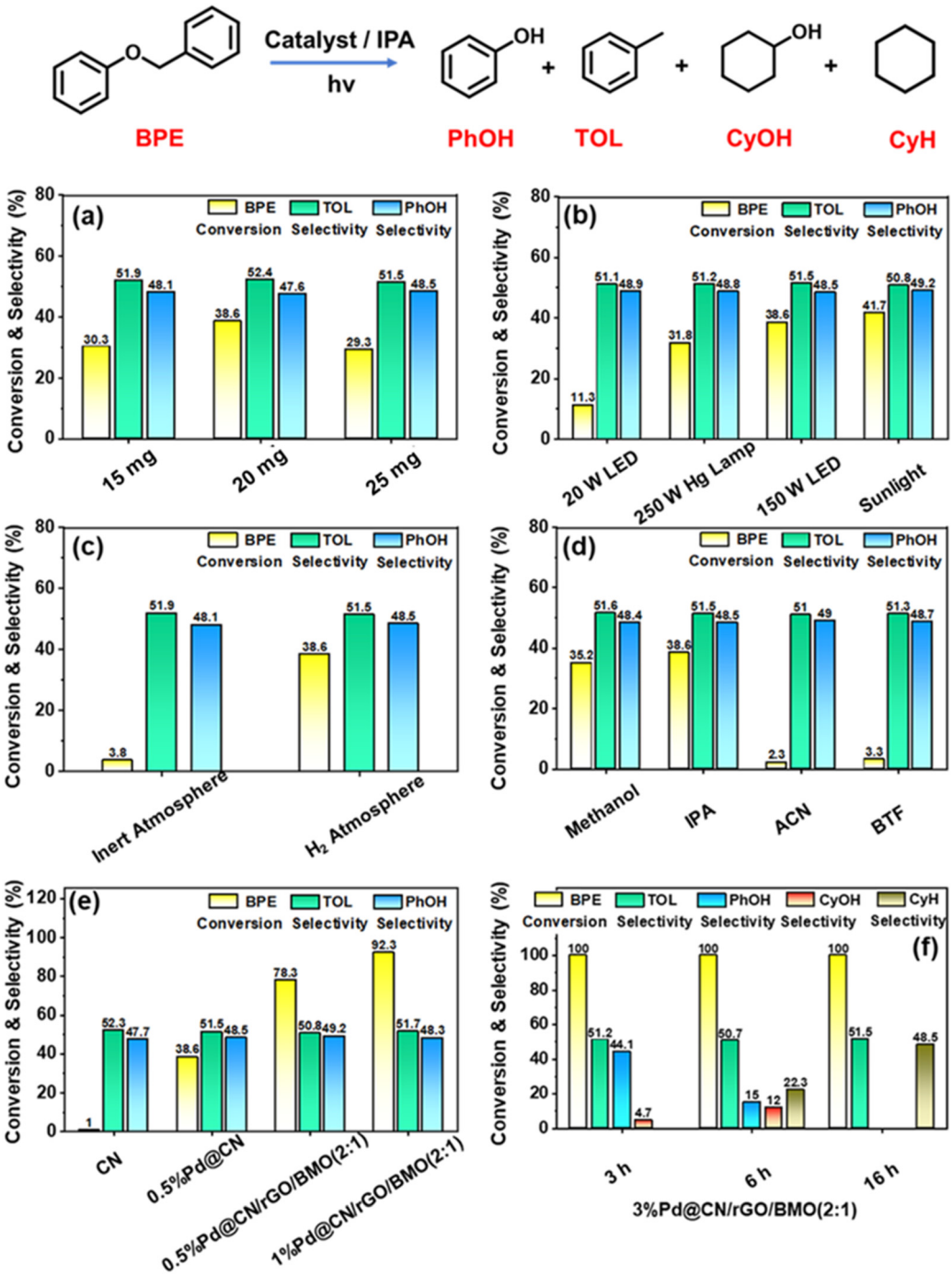

Fig. 7 BPE hydrogenolysis was conducted with systematic variations in the following parameters (a) photocatalyst in mg, (b) light-source, (c) reaction atmosphere, (d) solvents, (e) catalysts, and (f) time interval using 3%Pd@CN/rGO/BMO(2 : 1). (Reaction-conditions: light (150 W LED), catalyst amount (20 mg), BPE (0.1 mmol)), H_2 (2 bar), time 3 h, and IPA (5 ml).

BPE conversion rate at 41.7%, producing equimolar amounts of TOL and PhOH (10:30 am to 1:30 pm, October 2023, intensity = 1390 W m^{-2}). Conversely, a household 20 W LED yielded a modest 11.3% BPE conversion, while a 250 W Hg lamp yielded 31.8% conversion. A 150 W LED (intensity = 1210 W m^{-2}) and sunlight emerged as superior illumination sources, guiding subsequent investigations. However, sunlight was not utilized for further optimization due to its daily intensity variations.

An inert atmosphere provided negligible BPE conversion (Fig. 7c), and the concentration of BPE remained unchanged, indicating that the reactant was stable in the presence of light under an inert atmosphere (Ar atmosphere). Introducing isopropyl alcohol (IPA) slightly improved conversion. 20 mg of the 0.5% Pd@CN catalyst exhibited better activity in hydrogen, attributed to the dissociative-adsorption of hydrogen by Pd NPs, forming surface Pd–H species that efficiently cleaved the α-O-4 linkage during BPE hydrogenolysis. Furthermore, IPA scavenged holes in the photocatalytic reaction (more in the mechanism part).

A diverse range of solvents was employed to evaluate their impact on the photocatalyst activity (Fig. 7d). Protic-solvents, like methanol and IPA, were observed to act as hole scavengers, with IPA demonstrating superior reactivity. Conversely, aprotic solvents, like acetonitrile (ACN) and benzotrifluoride (BTF), yielded no discernible conversion. Consequently, IPA was preferred for subsequent investigations. Catalyst screening involved various photocatalysts synthesized in the study (Fig. 7e and S18a–c†). Pristine CN exhibited negligible BPE transformation (~1% conversion). However, introducing metal NP decorations, particularly Pd NPs, significantly enhanced BPE hydrogenolysis. While Co and Ni NP decorated CN displayed inferior performance, Pd NP-decorated samples excelled, with Ru NP decorated CN showing somewhat lower activity. The excellent performance of Pd can be ascribed to its intrinsic attributes, such as a lower Fermi level and higher work function, favoring efficient electron migration from the CN conduction band. To further enhance the conversion rate, a Z-scheme photocatalyst was strategically designed. The design combined CN as the reductive photocatalyst with BMO as the oxidative photocatalyst, utilizing reduced rGO as a mediator in the CN/rGO/BMO (1 : 1) configuration. The role of rGO as a mediator is discussed in the mechanism part. The configuration improved charge separation and achieved a remarkable 64.6% BPE conversion with 0.5% Pd loading with an AQY of 142 × 10^{-3} (Table S6†), generating equimolar TOL and PhOH products (Fig. S19a†).

After optimizing the quantities of CN and BMO within the heterojunction, optimal performance was achieved in the 0.5% Pd@CN/GO/BMO(2 : 1) configuration, resulting in a notable 78.3% BPE conversion with an equal content of TOL and PhOH after 3 h (Fig. S19b†). Thus, CN/GO/BMO(2 : 1) was identified as the most effective combination for the heterojunction. However, in the absence of Pd, the activity was low, demonstrating only a 6% conversion rate, underscoring the crucial role of Pd NPs in catalyzing the reaction (Fig. S19c†). Consequently, a gradual increase in the loading of Pd NPs over CN/GO/BMO(2 : 1) was undertaken. The 1% Pd catalyst reached 92.3% BPE conversion, while 3% Pd achieved full conversion in 3 h, achieving an impressive AQY value of 209 × 10^{-3} (Table S6†), showcasing an impressive feat of complete BPE cleavage. However, a higher Pd content also led to the emergence of a new product, cyclohexanol (CyOH), with the final product distribution settling at 51.2% TOL, 44.1% PhOH, and 4.7% CyOH (Fig. 7f). Extending the reaction to 6 h revealed a shift in product selectivity, with 50.7% TOL, 15% PhOH, 12% CyOH, and 22.3% cyclohexane (CyH) (Fig. 7f). It suggests the catalyst's ability to sequentially hydrogenate PhOH to CyOH, which undergoes further hydrogenation to CyH. After 16 h, a complete transformation of PhOH to CyH through the intermediate CyOH was observed. The evolved selectivity profile demonstrated a shift to 51.5% TOL and 48.5% CyH. Interestingly, the very large TOL remained unaltered, highlighting the catalyst's limitation in reducing the toluene ring. Control experiments involving TOL, PhOH, and CyOH as reactants were conducted under analogous conditions (Table S7†). The 3% Pd@CN/rGO/BMO(2 : 1) catalyst exhibited notable proficiency in reducing PhOH and CyOH. In contrast, TOL demonstrated insusceptibility to conversion under these conditions (time 4 h) (Table S7†). However, over a longer time span (time 16 h), a small amount of TOL was converted into methylcyclohexane (MCY) [conversion (9%)] (Table S7†). This discerning observation unequivocally establishes that, for achieving aromatic selectivity, the 0.5% Pd@CN/rGO/BMO(2 : 1) catalyst stands as the optimal choice. In contrast, 3% Pd@CN/rGO/BMO(2 : 1) emerged as the preferred option for fostering the production of TOL and CyH as primary products, demonstrating the catalyst's role in determining the product selectivity in the complex hydrogenolysis of BPE.

To probe the relationship between the catalyst's spectral response and its activity, reactions under optimized conditions were conducted using different coloured LED lights: violet (λ_{max} = 401 nm), blue (λ_{max} = 448 nm), green (λ_{max} = 520 nm), red (λ_{max} = 633 nm), and cool white (9 W each). The catalytic activity displayed a clear hierarchy, with violet light leading to the highest BPE conversion and red light yielding the lowest (Fig. S20†). This observed trend directly corresponds to the catalyst's light absorption characteristics, highlighting the importance of matching excitation wavelengths to maximize photocatalytic efficiency. Due to its wider availability, cool white light emitting in the 390 to 750 nm (λ_{max} = 455 nm) was chosen as the light source for the photocatalytic process.

Following an examination of the photocatalytic cleavage of the α-O-4 linkage, the subsequent pursuit involves extending the photocatalytic system to the β-O-4 linkage. Initially, 0.5% Pd@CN/rGO/BMO(2 : 1) was employed for cleavage under analogous reaction conditions. Given the higher bond-dissociation energy of the β-O-4 linkage in comparison to the α-O-4 linkage, a longer time of 16 h was necessary to achieve an 80.2% conversion with an AQY value of 32 × 10^{-3} (Table S8†). The resultant reaction yielded two primary products: 51.8% ethyl

benzene (EB) and 48.2% PhOH (Fig. 8a). Extending the reaction duration to 24 h resulted in full conversion, while the product selectivity remained unaltered (Fig. 8a). Subsequently, the reaction was repeated using the 1%Pd@CN/rGO/BMO (2 : 1) catalyst, yielding an enhanced conversion of 95.8% in 16 h, accompanied by the appearance of new products—ethyl

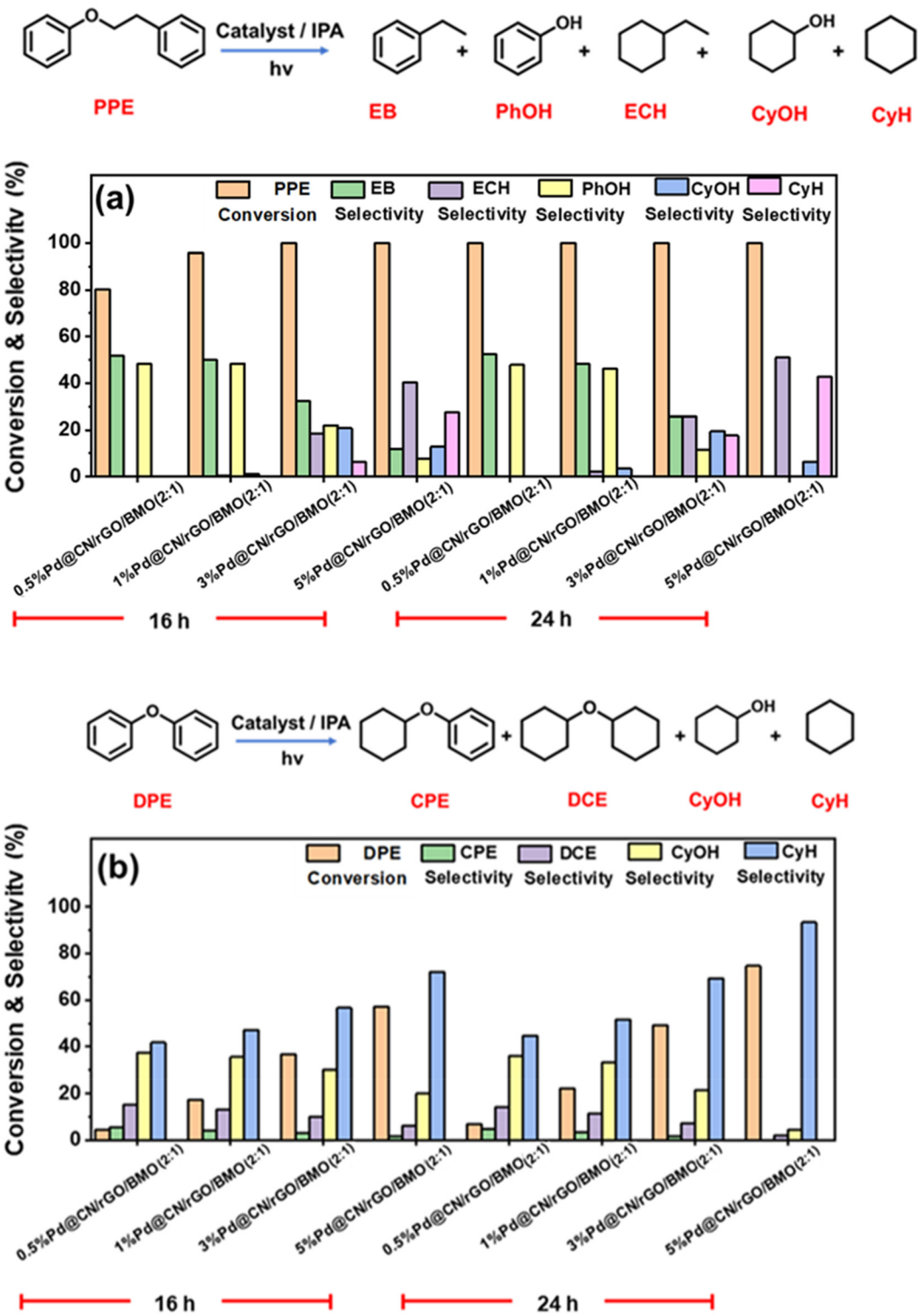

Fig. 8 (a) PPE hydrogenolysis was conducted with different catalysts and time interval. (Reaction-conditions: light (150 W LED), catalyst amount (20 mg), PPE (0.1 mmol)), H_2 (2 bar), and IPA (5 ml), and (b) DPE hydrogenolysis was conducted with different catalysts and time intervals. (Reaction-conditions: light (150 W LED), catalyst amount (20 mg), DPE (0.1 mmol)), H_2 (5 bar), and IPA (5 ml).

cyclohexene (ECH) and cyclohexanol (CyOH) in the reaction mixture (50% EB, 48.4% PhOH, 0.5 ECH, and 1.1 CyOH) (Fig. 8a). Increasing the Pd content led to the conversion of a very small portion of EB and PhOH into ECH and CyOH. Further optimization involved a subsequent increase in time to 24 h, resulting in 100% conversion with an increase in the formation of ECH and CyOH (Fig. 8a). The adjusted product selectivity included 48.2% EB, 46.2% PhOH, 2.1% ECH, and 3.5% CyOH (Fig. 8a). Elevating the Pd content to 3% aimed to enhance aliphatic product formation, achieving 100% conversion in 16 h with the best AQY (41×10^{-3}) (Fig. 8a). Aliphatic selectivity was increased, comprising 32.4% EB, 22.0% PhOH, 18.5% ECH, 20.8% CyOH, and 6.3% cyclohexane (CyH). Prolonging the reaction time to 24 h augmented the aliphatic selectivity to 25.7% for ECH and 17.6% for CyH (Fig. 8a). Further elevating the Pd content to 5% aimed to achieve complete aliphatic selectivity. In 16 h, a combined aliphatic selectivity of 80.7% (40.3% ECH, 12.9% CyOH, and 27.5% CyH) was attained (Fig. 8a). In the extended 24 h timeframe, complete aliphatic selectivity was realized. This delineates the process's capability to yield both aromatic and aliphatic products from the lignin model PPE. Notably, lower Pd content facilitates aromatic selectivity with substantial conversion, while higher Pd content and extended reaction time lead to the hydrogenation of aromatics into aliphatic products. The bond cleavage event generates EB and PhOH as primary products, which subsequently undergo hydrogenation to yield ECH and CyH. Experimental verification of this phenomenon involved the direct reaction of EB under similar conditions using 3% Pd@CN/GO/BMO(2 : 1) as the catalyst, resulting in a 95% conversion to ECH in 12 h (Table S7†).

Concurrently, attention was directed to another model compound with the β-O-4 linkage, PPEOL, which resembles the lignin polymer. The hydrogenolysis of PPEOL was more facile than PPE due to an additional functionality. Photocatalytic hydrogenation of PPEOL was conducted using 0.5%Pd@CN/GO/BMO(2 : 1) for 12 h, yielding 69.8% conversion and 100% aromatic selectivity (Fig. S21†). This reaction resulted in the formation of numerous aromatic compounds, including phenyl ethanol (PEA) (25.2%), PhOH (48.2%), styrene (STY) (4.5%), and EB (22.1%) (Fig. S21†). Optimal conversion with 100% aromatic selectivity was attained using 1%Pd@CN/GO/BMO(2 : 1) in 12 h (Fig. S21†). In this instance, 88.7% of PPEOL underwent conversion into aromatic products with a selectivity of 14.6% PEA, 49.5% PhOH, 3.2% STY, and 32.7% EB (Fig. S21†). Subsequently, the objective shifted towards achieving significant aliphatic selectivity in the hydrogenolysis of PPEOL. Systematic optimization of parameters such as loading amount and reaction time culminated in the realization of a peak combined aliphatic selectivity of 88.8% (39.6% ECH, 14.6% CyOH, and 34.6% CyH) with 5%Pd@CN/GO/BMO(2 : 1) after 16 h (Fig. S21†) attaining an AQY value of 41×10^{-3} (Table S9†). Consequently, both aliphatic and aromatic products were obtained through the photocatalytic hydrogenolysis of PPEOL.

Having successfully addressed the cleavage of α-O-4 and β-O-4 linkages, our focus shifted to the most challenging 4-O-5 linkage with the highest C–O bond dissociation energy. Diphenyl ether (DPE) was selected as the substrate for the photocatalytic cleavage of the 4-O-5 linkage. Initial attempts were made using the 0.5%Pd@CN/rGO/BMO(2 : 1) catalyst under analogous conditions, yielding no discernible conversion in the first 16 h. Subsequent adjustments, including augmenting Pd loading to 1% and 3%, failed to improve conversion significantly. To enhance reactivity, the hydrogen pressure was increased to 5 bar, resulting in a modest 4.6% conversion with the 0.5%Pd@CN/GO/BMO(2 : 1) catalyst over 16 h, accompanied by the formation of diverse products (Fig. 8b). Product selectivity for the reaction manifested as 5.6% CPE, 15.2% DCE, 37.4% CyOH, and 41.8% CyH (Fig. 8b). Initially, one ring undergoes hydrogenation, yielding the intermediate cyclohexyl phenyl ether (CPE). Subsequently, the second ring undergoes reduction, generating dicyclohexyl ether (DCE) as an intermediate. The subsequent cleavage of the C–O bond in DCE, results in the formation of two distinct products, CyOH and CyH. Given the initially low conversion, the reaction was extended to 24 h, yielding a marginally improved 7% conversion (Fig. 8b). To further optimize the conversion rate, Pd loading was increased to 1%, yielding 17.5% and 22.3% DPE conversion in 16 h and 24 h, respectively (Fig. 8b). A subsequent increase in Pd loading to 3% resulted in a further enhancement of conversion to 36.7% and 49.3% in 16 h and 24 h, respectively (Fig. 8b). Lastly, the reaction was conducted with 5%Pd@CN/rGO/BMO(2 : 1), yielding a substantial increase in conversion to 57.2% in 16 h, with a predominant 72.1% selectivity towards CyH with the best AQY (23×10^{-3}) (Table S10†). To maximize conversion, the reaction was extended to 24 h, achieving a DPE conversion of 74.6% with an impressive 93.4% selectivity for CyH (Fig. 8b).

Following the successful cleavage of model compounds, the photocatalytic system tackled lignin linkages in simulated bio-oil containing various linkages. The bio-oil incorporated lignin models (BPE, PPE, PPEOL, and DPE) in equimolar proportions. Under analogous photocatalytic conditions using the most effective catalyst, 5% Pd@CN/rGO/BMO(2 : 1), complete bio-oil conversion into monomers required 36 h. All products were identified through GCMS analysis (Fig. S8†). After 36 h, four products were obtained with a selectivity of 60.1% CyH, 26.1% ECH, 11.3% TOL, and 2.5% MCH. Additionally, the reaction was scrutinized at designated time intervals, revealing various intermediates such as EB, PhOH, CyOH, CPE, and DCE. Consequently, the photocatalytic system adeptly valorises bio-oil, converting it into utilizable monomers characterized by elevated aliphatic selectivity, with CyH emerging as the predominant product.

After achieving favourable outcomes with lignin models and simulated lignin bio-oil, raw lignin extracted from teak tree wood was investigated (Fig. 9). The lignin was obtained from teak wood sawdust (*Tectona grandis*) sourced from a local furniture shop, using a refluxing process with the IPA solvent and HCl catalyst (the detailed process is provided in the ESI†). Powder XRD and FT-IR analysis confirmed the successful extraction of lignin from hardwood with complete removal of

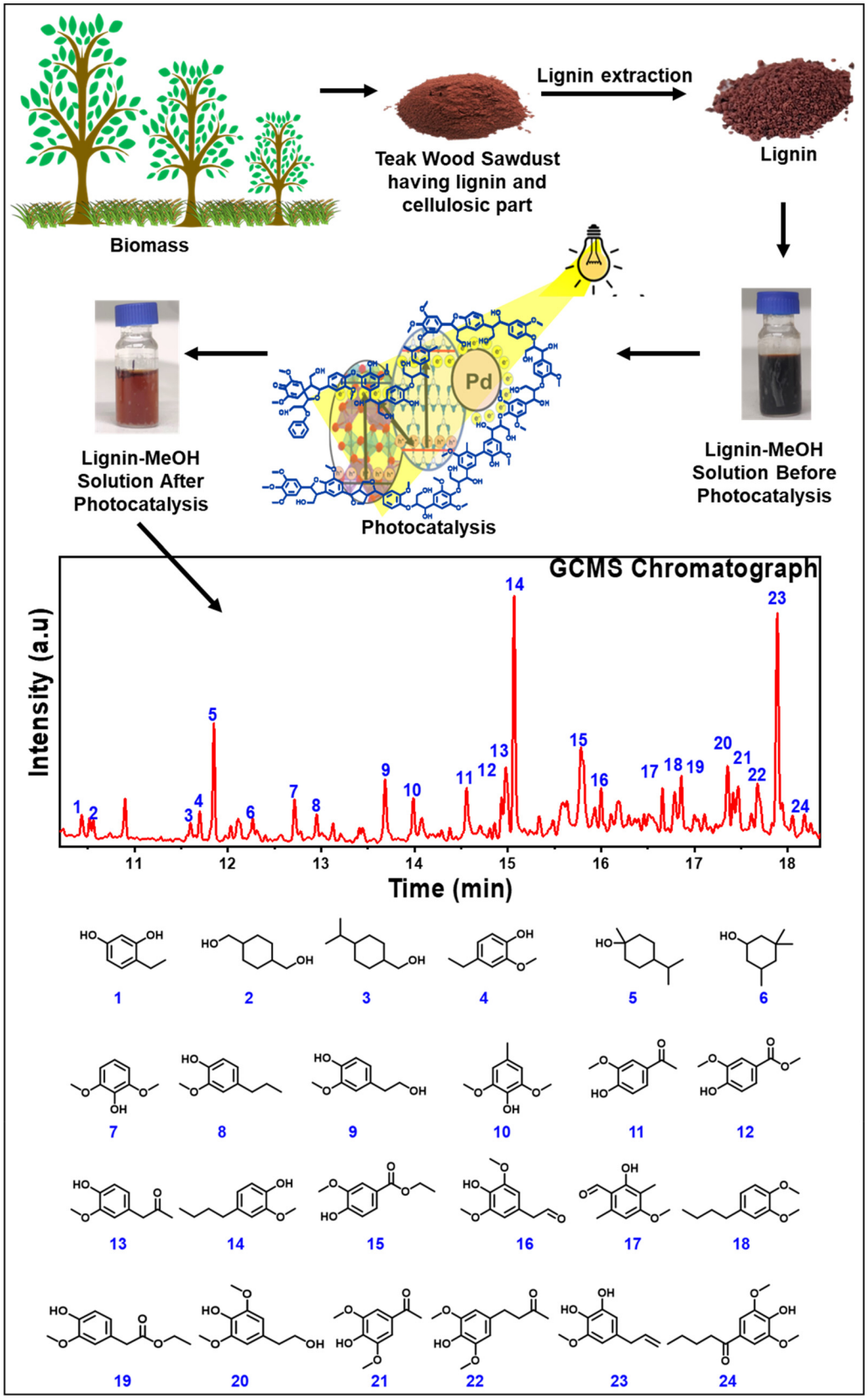

Fig. 9 The illustration depicts the photocatalytic process employed for the hydrogenolysis of native lignin extracted from teak wood sawdust, and the GC-MS chromatogram showcasing the obtained aromatic monomers.

the cellulosic part from the wood (Fig. S22, ESI†). Subsequently, the extracted lignin was employed in a photocatalytic reaction utilizing the optimal catalyst, 5% Pd@CN/rGO/BMO(2 : 1). The lignin extract was not completely miscible in the alcoholic solvent. To render the lignin extract soluble in methanol, 300 mg of lignin extract in 10 ml of MeOH was treated at 180 °C for 2 h. Following treatment, 78% of the lignin extract became soluble, while the remaining residue was filtered. Methanol was chosen for the thermolytic solvolysis of lignin in alcoholic solvents because of its best efficiency in the literature.[73] Before the photocatalytic reaction, a GC-MS analysis of the reaction mixture was conducted (Fig. S23†). The photocatalytic reaction was carried out for 24 h with a 150 W LED. After the reaction, GC-MS analysis of the reaction mixture was performed and compared with the GC-MS of the original reaction mixture (Fig. S23†). Post-photocatalytic reaction, there was an increase in the variety and concentrations of aromatic monomers (Fig. 9 and S23†). The GC-MS analysis revealed the emergence of new peaks (1, 7, 8, 9, 10, 12, 13, 14, 17, 18, 19, 20, 21, and 22) in the chromatogram, along with an augmented prominence of existing peaks (2, 3, 4, 5, 6, 11, 15, 16, 23, and 24) (Fig. 9 and S23†). The discernible peaks correspond to approximately 24 different identifiable aromatic monomers, including 1,4-cyclohexanedimethanol, cyclohexanemethanol, 4-(1-methylethyl)-, homovanillyl alcohol, acetovanillone, guaiacol, 4-butyl-syringylacetone, and 6-hydroxyeugenol (Fig. S24†). Given the complexity of lignin, numerous products are anticipated after the photocatalytic reaction. 5% Pd@CN/rGO/BMO(2 : 1) demonstrated photocatalytic conversion of native lignin through hydrogenolysis, producing various monomers. It underscores the effectiveness of the photocatalytic system in producing monomers from natural lignin.

The photocatalytic system for lignin valorization was assessed through a comprehensive comparison with the existing literature. Despite the absence of a single system capable of simultaneously cleaving all three major lignin ether linkages (α-O-4, β-O-4, and 4-O-5), individual assessments were carried out for each linkage. In the case of α-O-4 cleavage, previous studies (utilizing 2.5Au-ASN-Ni^{2+} and TiN NPs) required high temperatures (~100 °C) and the addition of a base (KOH), resulting in low conversion rates and exclusively aromatic products (Table S11†).[26,27] The present study achieved complete conversion at room temperature without any additive, offering control over product selectivity between aromatics and ring-reduced options. Similarly, for the β-O-4 cleavage, earlier investigations using $ZnIn_2S_4$, CdS, Ni/CdS, and $Cd_xZn_{1-x}S$ exclusively yielded aromatic products (Table S12†).[16–24] In contrast, our catalytic system demonstrated the selective production of aromatic and aliphatic ring-reduced products through photocatalytic hydrogenolysis at room temperature, marking a pioneering achievement in the field. While previous reports for 4-O-5 cleavage relied on methods such as employing 4%Pt(P25)@TiO_2 under UV light and with the assistance of strong acid HCl (1.2 equivalents) for cleaving 4-O-5 linkages,[28] our study stands out as the first to achieve photocatalytic cleavage of this elusive linkage at room temperature without any additives, aligning perfectly with the principles of green chemistry. Furthermore, we demonstrated the photocatalytic valorization of a mixture of α-O-4, β-O-4, and 4-O-5 in producing liquid fuels, which is not reported under photocatalytic conditions.

Photocatalytic reaction mechanism

During heterojunction formation in CN/rGO/BMO(2 : 1), the Fermi levels of CN (4.58 eV *vs.* V_{ac}) and BMO (4.92 eV *vs.* V_{ac}) adjust to reach a new equilibrium at 4.72 eV *vs.* V_{ac}, as confirmed through the UPS experiment (Fig. S18a†). This equilibrium induces upward band bending within the CN and downward in BMO (Fig. 10a(i) and (ii)). This mechanism results in a distinct Fermi level of 4.72 eV *vs.* V_{ac} for the nanocomposite. Literature reports the Fermi level of Pd NPs at 5.12 eV *vs.* V_{ac}. Upon Pd NP incorporation onto the heterojunction, the combined system again reaches a new Fermi level equilibrium. This new level is 4.78 eV *vs.* V_{ac} for 0.5%Pd@CN/rGO/BMO(2 : 1) and 4.93 eV *vs.* V_{ac} for 5%Pd@CN/rGO/BMO(2 : 1) catalysts (Fig. 6e). Because the work-function (Φ) of Pd is higher than that of CN/rGO/BMO(2 : 1), the photogenerated electrons readily migrate from the heterojunction's conduction band (CB) to the Pd NPs.

The combined data from DRUV, MS, VB-XPS, and UPS experiment suggest a Type-II or Z-scheme heterojunction formation in CN/rGO/BMO(2 : 1) (Fig. 10b), likely underpinning its boosted activity. Under light irradiation, CN and BMO generate charge carriers in their conduction and valence bands, giving rise to two potential charge transfer mechanisms: Type-II and Z-scheme (Fig. 10b). In the Type-II arrangement, holes from BMO's valence bands migrate to CN's valence bands, while electrons from CN's conduction bands move to BMO's conduction bands, leading to oxidation at CN and reduction at BMO. Alternatively, the Z-scheme involves recombination of holes and electrons at the interface, followed by oxidation at BMO's VB and reduction at CN's conduction bands. To confirm the prevailing mechanism, control experiments were conducted. The Nitro Blue Tetrazolium (NBT) test confirmed the photocatalyst's ability to generate superoxide radicals from molecular oxygen, requiring a reduction potential of −0.33 V *vs.* NHE. BMO's conduction band position falls below this threshold, rendering it incapable of superoxide generation, as observed in the NBT test (Fig. S25a†). In contrast, the conduction band position of CN is more negatively situated than the required reduction potential for superoxide formation, enabling significant superoxide production. Within the composite material, two distinct possibilities emerge (i) reduction at the conduction band of BMO (Type II), and (ii) reduction at the conduction band of CN (Z-scheme) (as illustrated in Fig. 10b). The NBT test (Fig. S25a†) confirms the effective generation of superoxide at the heterojunction, validating the reduction occurring at the conduction band of CN and thus establishing the Z-scheme nature of the CN/rGO/BMO(2 : 1) heterojunction. Similarly, to assess the photocatalyst's ability to create OH radicals, a terephthalic acid (THA) test was performed using PL spectroscopy (Fig. S25b†).[74] OH radical gene-

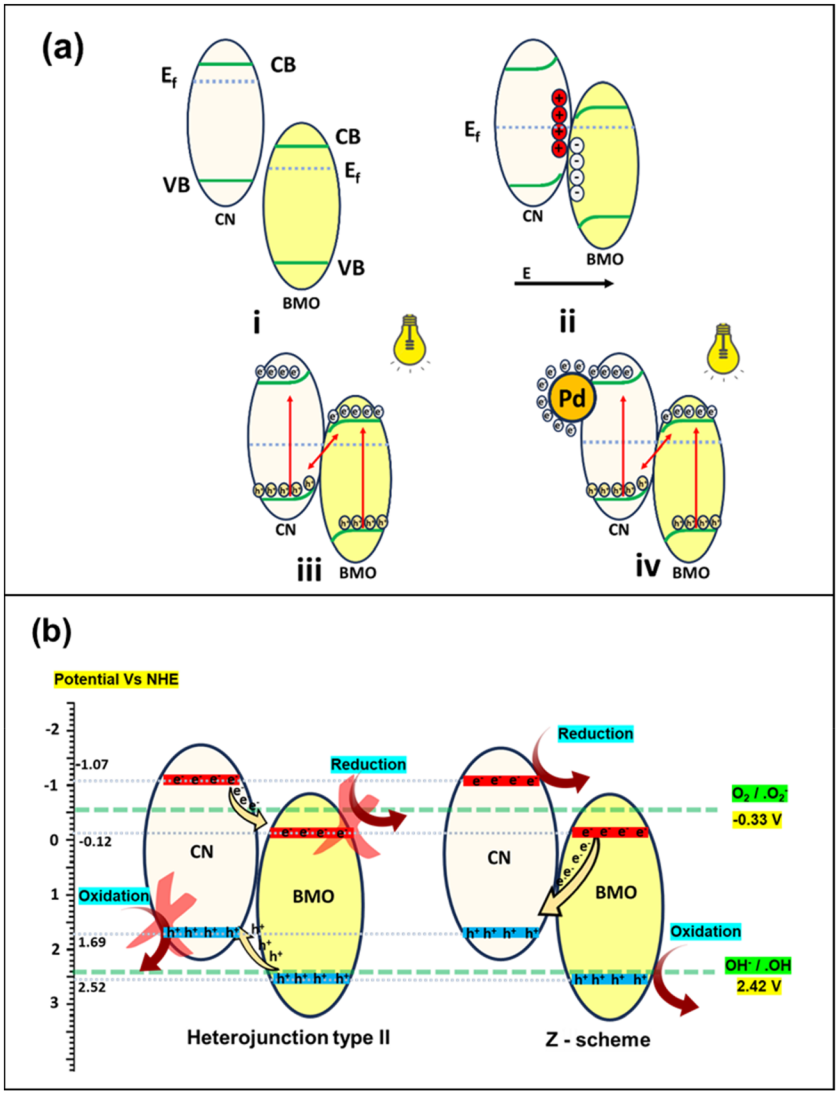

Fig. 10 (a) Band-structure for CN and BMO (i) without contact and (ii) with contact causing band-bending (iii) charge generation in composite CN/rGO/BMO in light and (iv) charge migration in Pd@CN/rGO/BMO in light. (b) Possible charge migration mechanism in CN/BMO, (i) type II and (ii) Z-scheme.

ration requires an oxidation potential of 2.42 V *vs.* NHE.[75,76] While CN's VB position does not meet this requirement, while BMO's does. The terephthalic acid test confirmed BMO's effective OH radical production (Fig. S25b†). Additionally, the test indicated that the heterojunction efficiently generated OH radicals with strong PL spectrum emissions, validating oxidation at BMO's VB. This reinforces the heterojunction's alignment with the Z-scheme configuration (Fig. 10b).

To comprehend the role of reduced rGO as the mediator in the Z-scheme charge transfer mechanism between CN and BMO, several control analyses were conducted. Heterojunctions between CN and BMO were fabricated with varying weights of the rGO precursor, *i.e.*, GO, including concentrations of 0%, 0.5%, 2%, and 5%. The effectiveness of rGO as the mediator in the charge transfer mechanism was assessed through analyses designed to discern charge separation and migration dynamics, including PL and transient on–off photocurrent measurements, across the spectrum of rGO variations in the CN/rGO/BMO(2 : 1) heterojunction (Fig. S26†). The findings conclusively demonstrated that heterojunctions incorporating rGO exhibited better charge separation and diminished charge recombination rates than their counterparts without rGO (Fig. S26a†). Consequently, rGO promotes the Z-scheme charge transfer, improving the charge carrier lifetime, as evidenced by the enhancement in the on–off current (Fig. S26a†) and a decrease in emission intensity (Fig. S26b†). Furthermore, the examination of PL and on–off data from heterojunctions featuring diverse rGO variations revealed the optimal weight percentage of GO (rGO precursor) to be 2%. This optimization underscores the critical role of rGO in orchestrating an efficient Z-scheme charge transfer mechanism within the CN/rGO/BMO(2 : 1) heterojunction.

A series of control experiments were undertaken to elucidate the role of charged particles in the photocatalytic hydrogenolysis of BPE using the 3% Pd@CN/rGO/BMO(2 : 1) Z-scheme heterojunction catalyst. Initially, the impact of light was assessed by conducting the reaction in the dark (Fig. S27a†). No conversion was observed at room temperature, but upon elevating the temperature above 120 °C, the catalyst exhibited activity, albeit at a reduced conversion rate (Fig. S27a†). However, a higher temperature resulted in a higher conversion rate (Fig. S27a†). A non-photoactive support, SBA-15, was employed to investigate the photocatalytic component's role in the reaction. Pd NPs embedded SBA-15 exhibited no activity in light, indicating that Pd NPs alone did not activate hydrogen by light alone; a photoactive component was required (Fig. S27b†). In this context, the Z-scheme heterojunction served this purpose. Although Pd over SBA-15 exhibited activity, a higher temperature (140 °C) was necessary in the absence of light (Fig. S27b†).

The photocatalytic process occurred upon electron and hole generation, an exploration of this aspect was imperative. BPE hydrogenolysis in the presence of electron scavengers, such as CCl_4 and formic acid, resulted in a decrease in BPE hydrogenolysis, underscoring the pivotal role of electrons in the process (Fig. S27c†). IPA functioned as a hole scavenger, as evidenced by successful hydrogenolysis in its presence. Substituting IPA with a non-aprotic solvent like acetonitrile (ACN) yielded unsatisfactory results, underscoring the unique relevance of IPA (Fig. S27d†). To confirm the importance of a hole scavenger, the external scavenger triethanolamine (TEA) was added to ACN. TEA addition successfully facilitated the hydrogenolysis of BPE in ACN with added TEA, affirming the need for a hole scavenger in the photocatalytic reaction (Fig. S27d†). In the absence of IPA, BPE hydrogenolysis occurred due to the H_2 gas, indicating the role of hydrogen in the reduction process. Nevertheless, IPA played a pivotal role in suppressing hole accumulation, increasing electron availability, and activating the catalyst when incorporated into ACN and other solvents. Increasing the concentration of IPA correlated with a higher BPE conversion, emphasizing the critical role of managing hole concentrations to ensure sufficient supply of electrons for the dissociation of Pd–H from the surface for the cleavage of BPE (Fig. S27d†). Furthermore, after consuming holes, IPA underwent conversion into acetone with the liberation of hydrogen, as observed in the GC profiles of the reaction mixture (Fig. S9†).

Although IPA provides hydrogen, molecular hydrogen remains the primary source of hydrogen for the reaction, experimentally confirmed by conducting the photocatalytic reaction under different pressures of H_2 (Fig. S28a†). Without H_2, the conversion rate was low (~6%). Therefore, IPA was inefficient in providing hydrogen required for the reaction. The introduction of molecular hydrogen enhanced the conversion. Moreover, with an increase in the H_2 concentration, hydrogenolysis was facilitated, indicating the importance of H_2 for the reaction (Fig. S28a†). In the photocatalytic reaction, there is a possibility of the formation of different radical species. To explore the radical species, some control experiments were performed. The reaction was conducted under a hydrogen atmosphere, minimizing the possibility of oxygenated radicals like hydroxyl (OH) and superoxide radicals; scavenging experiments were performed to prove such a phenomenon. The presence of OH radicals was probed using methanol (MeOH) and *tert*-butyl alcohol (TBA) as scavengers (Fig. S28b†). The conversion remained unchanged, indicating minimal involvement of OH radicals in the reaction system. Similarly, scavenging experiments were conducted using hydroquinone (HQ) and benzoquinone (BQ) to detect the superoxide radicals (Fig. S28c†). These tests yielded negative results, ruling out the possibility of the formation of superoxide radicals.

Radical generation from the reactants is also possible through C–H bond activation aided by photogenerated holes. IPA utilizes the photogenerated holes, making the chances of C–H activation of reactant molecules scarce. To validate this hypothesis, the scavenging study was performed using DMPO and TEMPO as radical scavengers. The unchanged conversion rate in these experiments indicated that radicals were not formed by the C–H activation of the reactant (Fig. S28d†). Interestingly, GC-MS analysis of the reaction mixture containing DMPO as a scavenger revealed the trapping of radicals derived from IPA (Fig. 11a). It confirms IPA utilization to scavenge the photogenerated holes, converting itself into radicals subsequently trapped by DMPO (Fig. 11a). The O–H bond of the IPA is activated by the holes which generate $(CH_3)_2CH\text{-}O^{\bullet}$ and H^+. Another H^+ was liberated from $(CH_3)_2CH\text{-}O^{\bullet}$, converting it into acetone, which was detected by GC (discussed previously). The absence of adducts like DMPO-OH in GC-MS of the photocatalytic reaction with DMPO confirmed that other radical species like OH radicals were not involved in the reaction. Similar scavenging experiments were conducted for the photocatalytic dissociation of β-O-4 and 4-O-5 linkages, establishing the crucial roles of electron and hole scavengers through these control reactions (Fig. S29 and S30†).

The comprehensive mechanistic illustration of the photocatalytic hydrogenolysis of BPE is depicted in Fig. S31.† The photocatalyst absorbs the incident light, initiating charge separation according to the Z-scheme mechanism outlined previously. Pd NPs adsorb molecular hydrogen on their surface. Given the lower Fermi level of the Pd NPs related to the heterojunction, electrons from the conduction band of the heterojunction transfer to the Pd NPs, facilitating the desorption of hydrogen from the Pd surface. Concurrently, holes are generated over the valence band of the catalyst. These holes interact with IPA, catalyzing its transformation into acetone with the concomitant liberation of hydrogen (Fig. S31†). Simultaneously, BPE interacts with the catalyst, where the hydrogen from the surface of the Pd NPs transfers to the C–O bond, resulting in the dissociation of BPE into TOL and PhOH (Fig. S31†). When a higher concentration of Pd NPs is present in the catalyst, the double bond of PhOH undergoes reduction, leading to its conversion into CyH through CyOH as an intermediate. The control reaction with TOL also confirmed that

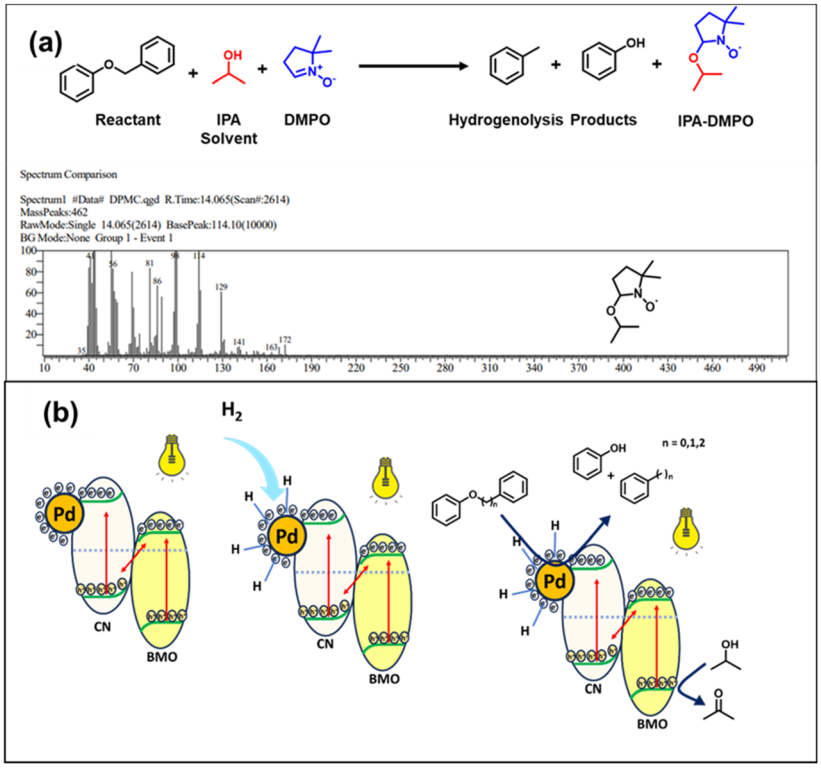

Fig. 11 (a) The trapping of the IPA radical generated through OH activation of IPA in the presence of DMPO and (b) possible reaction mechanism for photocatalytic hydrogenolysis of lignin ethers over Pd@CN/rGO/BMO.

under the optimized conditions, TOL was not reduced in lower time.

The dissociation of the β-O-4 linkage follows a similar pathway, as depicted in Fig. S32,† yielding EB and PhOH as the predominant products. Molecular H_2 acts as the primary hydrogen source, while simultaneously IPA consumes the photogenerated hole, converting itself into the $(CH_3)_2CH\text{-}O^{\bullet}$ radical with the liberation of H^+. With the assistance of another hole, $(CH_3)_2CH\text{-}O^{\bullet}$ converts into acetone. The photogenerated electrons migrates over the Pd NPs due to their low Fermi level, facilitating the dissociation of adsorbed Pd–H, which cleaves the β-O-4 linkage, converting the reactants into EB and PhOH. Catalysts with a higher Pd content exhibited a greater capability for hydrogenation. In configurations with higher Pd concentrations, hydrogen from the surface of Pd NPs migrates to the double bonds in the ring of EB and PhOH, effectively reducing these compounds into ECH and CyH.

The hydrogenolysis of the 4-O-5 linkage proceeded differently and required a higher amount of Pd (Fig. S33†). Molecular H_2 is the primary hydrogen source, while IPA converts into acetone by consuming the photogenerated holes. Initially, one ring of diphenyl ether (DPE) undergoes reduction, transforming it into cyclohexyl phenyl ether (CPE), observed in GC-MS chromatography (Fig. S7†). Subsequently, the other ring undergoes reduction, forming dicyclohexyl ether (DCE) as an intermediate. After the reduction of both rings, the catalyst successfully cleaves the C–O bond, generating CyOH and CyH as the final products of the reaction (Fig. S33†). With prolonged reaction time, CyOH was reduced into CyH (Fig. S33†). Consequently, this reaction yielded a single product, CyH, with high selectivity.

In light of the well-established comprehension of the role played by the composite catalyst, a thorough exploration into the significant contribution of Pd was crucial, considering its influence on catalytic activity. Pd NPs play a central role in this context, helping the dissociative adsorption of H_2 and their proficient ability to accept and accommodate photogenerated electrons. An experiment designed to validate this hypothesis utilized a non-photocatalytic material, SBA-15, which cannot generate charge carriers. Under a 150 W LED, the 3% Pd-decorated SBA-15 exhibited minimal activity for the hydrogenolysis of BPE at room temperature (Fig. S27b†). This result emphasizes that, without photogenerated electrons, Pd NPs struggled to facilitate hydrogen molecule desorption under ambient conditions. As a result, it can be inferred that the photocatalyst absorbs light, initiating the formation of electron–hole pairs (Fig. 11b). The holes are quenched by IPA, while the electrons are accepted by Pd NPs, aiding in the liberation of absorbed hydrogen (Pd–H) and subsequent hydrogenolysis of various lignin models (Fig. 11b). Under illumination, charge carriers emerge on the photocatalyst's surface. Pd NPs efficiently adsorb molecular H_2. XPS and UPS analyses confirmed the Pd NPs' capability to hold and accommodate photogenerated electrons from the conduction band of the Z-scheme photo-

catalyst. This phenomenon is attributed to the optimum work function (approximately 5.12 eV) and Fermi energy level of the Pd NPs. A Schottky barrier at the interfaces between the conduction band and Pd NPs creates favourable energy circumstances for the smooth transfer of electrons.

Recyclability experiments were conducted to evaluate the photocatalyst's performance over five catalytic cycles. The catalyst exhibited significant reusability throughout all successive runs (Fig. S34a†). Following each cycle, the photocatalyst was recovered *via* centrifugation, washed with ethanol, and dried overnight. The catalyst demonstrated consistent stability across the photocatalytic recyclability test, with no observable decrease in activity. To evaluate the stability of the spent catalyst, various characterization techniques were employed. XRD analysis revealed a similar structure for the spent catalyst compared to the fresh catalyst (Fig. S34b†). Moreover, XPS analysis confirmed the stability of the Pd NPs, demonstrating a similar elemental composition with Pd predominantly in the metallic form (Pd^0) (Fig. S34c and d†). To assess potential changes in optical properties after five reaction cycles, DR-UV and on–off photocurrent analyses were conducted (Fig. S34e and f†). The results indicated that the spent catalyst retained optical properties identical to the fresh catalyst.

Conclusions

In conclusion, the study successfully introduced a novel Pd@CN/rGO/BMO Z-scheme photocatalyst and demonstrated a green approach for sustainable lignin valorization. By eliminating harsh chemicals and harnessing visible light, the developed catalyst addresses key challenges associated with traditional methods. Through detailed characterization, including VB-XPS and UPS analyses of the Pd@CN/rGO/BMO(2 : 1) catalyst, the Z-scheme configuration was confirmed, and a band structure was established, showcasing significant enhancements in charge separation efficiency. The incorporation of Pd NPs enhanced charge separation and migration, with 5%Pd@CN/rGO/BMO(2 : 1) demonstrating exceptional effectiveness. 3%Pd@CN/rGO/BMO(2 : 1) demonstrated remarkable performance, achieving complete conversion of BPE with 100% aromatic selectivity in 3 h and 100% aliphatic selectivity in 16 h. Similarly, for PPE, 3%Pd@CN/rGO/BMO (2 : 1) achieved 100% conversion with 100% aromatic selectivity in 16 h, while 5%Pd@CN/rGO/BMO(2 : 1) showed 100% aliphatic selectivity in 24 h, with DPE primarily yielding CyH with 77% conversion after 24 h. Notably, the catalyst displayed consistent and high selectivity across various organic substrates, emphasizing its practical utility. Supported by control experiments and thorough photoelectrochemical characterization, the proposed reduction mechanism highlights the crucial roles of Pd NPs and the Z-scheme configuration in driving catalytic activity. Moreover, the 5%Pd@CN/rGO/BMO (2 : 1) catalyst exhibited remarkable efficacy with simulated bio-oil, achieving nearly complete conversion with predominantly aliphatic products after 36 h. 5%Pd@CN/rGO/BMO (2 : 1) demonstrated the capability of producing monomers by the photocatalytic hydrogenolysis of native lignin extracted from teak wood sawdust. This research not only advances the understanding of photocatalysis mechanisms, but also underscores the pivotal roles of Pd NPs and Z-scheme configurations in sustainable lignin valorization.

Author contributions

The research was conceptualized by RS and RG. Experimental work was carried out, and all data were collected by RG. The manuscript is co-written by RG and RS.

Conflicts of interest

There are no conflicts to declare.

Acknowledgements

R. S. and R. G. express gratitude to SERB for funding (CRG/2020/000028). R. G. expresses gratefulness to CSIR, New Delhi, (09/1005(0031)/2020-EMR-I) for the fellowship. We also extend our appreciation to the Central Research Facility at IIT Ropar and SAIF IIT Bombay for their support in TCPCS analysis. Furthermore, the authors would like to thank Dr Rajaram Bal for TEM analysis.

References

1 S. H. Ghaffar and M. Fan, *Biomass Bioenergy*, 2013, **57**, 264–279.
2 J. Xu, C. Li, L. Dai, C. Xu, Y. Zhong, F. Yu and C. Si, *ChemSusChem*, 2020, **13**, 4284–4295.
3 Y. Pu, S. Cao and A. J. Ragauskas, *Energy Environ. Sci.*, 2011, **4**, 3154.
4 S. Gazi, *Appl. Catal., B*, 2019, **257**, 117936.
5 A. Kumar and R. Srivastava, *Sustainable Energy Fuels*, 2023, **7**, 5714–5732.
6 X. Wu, N. Luo, S. Xie, H. Zhang, Q. Zhang, F. Wang and Y. Wang, *Chem. Soc. Rev.*, 2020, **49**, 6198–6223.
7 L. I. Granone, F. Sieland, N. Zheng, R. Dillert and D. W. Bahnemann, *Green Chem.*, 2018, **20**, 1169–1192.
8 S.-H. Li, S. Liu, J. C. Colmenares and Y.-J. Xu, *Green Chem.*, 2016, **18**, 594–607.
9 S. Gillet, M. Aguedo, L. Petitjean, A. R. C. Morais, A. M. da Costa Lopes, R. M. Łukasik and P. T. Anastas, *Green Chem.*, 2017, **19**, 4200–4233.
10 W. Qu, X. Han, J. Liu, L. Yin, C. Liang and P. Hu, *Green Chem.*, 2023, **25**, 9873–9883.
11 R. Hu, J. Zhan, Y. Zhao, X. Xu, G. Luo, J. Fan, J. H. Clark and S. Zhang, *Green Chem.*, 2023, **25**, 8970–9000.
12 X. Liu, X. Duan, W. Wei, S. Wang and B.-J. Ni, *Green Chem.*, 2019, **21**, 4266–4289.

13 Z. Xiang, W. Han, J. Deng, W. Zhu, Y. Zhang and H. Wang, *ChemSusChem*, 2020, **13**, 4199–4213.
14 J. Xu, P. Zhou, C. Zhang, L. Yuan, X. Xiao, L. Dai and K. Huo, *Green Chem.*, 2022, **24**, 5351–5378.
15 D. Dai, J. Qiu, G. Xia, Y. Tang and J. Yao, *ACS Catal.*, 2023, **13**, 14987–14995.
16 J. Lin, X. Wu, S. Xie, L. Chen, Q. Zhang, W. Deng and Y. Wang, *ChemSusChem*, 2019, **12**, 5023–5031.
17 N. Luo, M. Wang, H. Li, J. Zhang, T. Hou, H. Chen, X. Zhang, J. Lu and F. Wang, *ACS Catal.*, 2017, **7**, 4571–4580.
18 S. Shao, K. Wang, J. B. Love, J. Yu, S. Du, Z. Yue and X. Fan, *Chem. Eng. J.*, 2022, **435**, 134980.
19 J. Xu, F. Lin, J. Wang and Y. Wang, *Chem. Phys. Lett.*, 2022, **805**, 139981.
20 G. Han, T. Yan, W. Zhang, Y. C. Zhang, D. Y. Lee, Z. Cao and Y. Sun, *ACS Catal.*, 2019, **9**, 11341–11349.
21 J.-Y. Wang, Z.-Z. Hu, X.-T. Sun, Y.-Q. Gao, J.-L. Wang, J. Xu and G. Jin, *Surf. Interfaces*, 2023, **36**, 102505.
22 H. Yoo, M.-W. Lee, S. Lee, J. Lee, S. Cho, H. Lee, H. G. Cha and H. S. Kim, *ACS Catal.*, 2020, **10**, 8465–8475.
23 J. Xu, M. Li, J. Qiu, X.-F. Zhang and J. Yao, *Int. J. Biol. Macromol.*, 2021, **185**, 297–305.
24 Y. Liu, Y. Guo, B. Lin, Z. Chen, X. Ying, M. Zhang, C. Wang, G. Zhang, H. Gu, D. Luo and X. Liu, *ACS Appl. Nano Mater.*, 2023, **6**, 6614–6626.
25 N. Luo, M. Wang, H. Li, J. Zhang, H. Liu and F. Wang, *ACS Catal.*, 2016, **6**, 7716–7721.
26 P. Han, T. Tana, Q. Xiao, S. Sarina, E. R. Waclawik, D. E. Gómez and H. Zhu, *Chem*, 2019, **5**, 2879–2899.
27 Z. Liu, Y. Huang, G. Xiao, P. Li, H. Su, S. Sarina and H. Zhu, *Energy Fuels*, 2021, **35**, 13315–13324.
28 Z. Peng, Z. Wu, X. Sun and H. Li, *Green Chem.*, 2023, **25**, 6869–6880.
29 E. Yilgor, G. E. Atilla, A. Ekin, P. Kurt and I. Yilgor, *Polymer*, 2003, **44**, 7787–7793.
30 C. Hu, X. Chen, Q. Dai, M. Wang, L. Qu and L. Dai, *Nano Energy*, 2017, **41**, 367–376.
31 R. Ghalta, A. K. Kar and R. Srivastava, *Chem. – Asian J.*, 2021, **16**, 3790–3803.
32 R. Ghalta and R. Srivastava, *Catal. Sci. Technol.*, 2023, **13**, 1541–1557.
33 J. Yu, G. Dai and B. Huang, *J. Phys. Chem. C*, 2009, **113**, 16394–16401.
34 A. Mishra, G. Bera, P. Mal, G. Padmaja, P. Sen, P. Das, B. Chakraborty and G. R. Turpu, *Appl. Surf. Sci.*, 2019, **488**, 221–227.
35 Z. Jia, F. Lyu, L. C. Zhang, S. Zeng, S. X. Liang, Y. Y. Li and J. Lu, *Sci. Rep.*, 2019, **9**, 7636.
36 R. Ghalta and R. Srivastava, *Sustainable Energy Fuels*, 2023, **7**, 1707–1723.
37 R. Ghalta, R. Bal and R. Srivastava, *Green Chem.*, 2023, **25**, 7318–7334.
38 Z. Zhang, T. Zheng, J. Xu and H. Zeng, *J. Mater. Sci.*, 2016, **51**, 3846–3853.
39 R. Bhosale, S. Jain, C. P. Vinod, S. Kumar and S. Ogale, *ACS Appl. Mater. Interfaces*, 2019, **11**, 6174–6183.
40 X. Xu, N. Yang, P. Wang, S. Wang, Y. Xiang, X. Zhang, X. Ding and H. Chen, *ACS Appl. Mater. Interfaces*, 2020, **12**, 1867–1876.
41 H.-C. Ma, J.-L. Kan, G.-J. Chen, C.-X. Chen and Y.-B. Dong, *Chem. Mater.*, 2017, **29**, 6518–6524.
42 X. Su, A. Vinu, S. S. Aldeyab and L. Zhong, *Catal. Lett.*, 2015, **145**, 1388–1395.
43 A. Chauhan, R. Ghalta, R. Bal and R. Srivastava, *J. Mater. Chem. A*, 2023, **11**, 11786–11803.
44 K. J. Samdani, J. H. Park, D. W. Joh and K. T. Lee, *ACS Sustainable Chem. Eng.*, 2018, **6**, 16702–16712.
45 J. Lv, J. Zhang, J. Liu, Z. Li, K. Dai and C. Liang, *ACS Sustainable Chem. Eng.*, 2018, **6**, 696–706.
46 M. Zhang, C. Shao, J. Mu, X. Huang, Z. Zhang, Z. Guo, P. Zhang and Y. Liu, *J. Mater. Chem.*, 2012, **22**, 577–584.
47 L. Ma, H. Fan, K. Fu, S. Lei, Q. Hu, H. Huang and G. He, *ACS Sustainable Chem. Eng.*, 2017, **5**, 7093–7103.
48 G. Collins, M. Blömker, M. Osiak, J. D. Holmes, M. Bredol and C. O'Dwyer, *Chem. Mater.*, 2013, **25**, 4312–4320.
49 A. S. Sharma and H. Kaur, *New J. Chem.*, 2018, **42**, 18935–18941.
50 G. Algara-Siller, N. Severin, S. Y. Chong, T. Björkman, R. G. Palgrave, A. Laybourn, M. Antonietti, Y. Z. Khimyak, A. V. Krasheninnikov, J. P. Rabe, U. Kaiser, A. I. Cooper, A. Thomas and M. J. Bojdys, *Angew. Chem.*, 2014, **126**, 7580–7585.
51 X. Wang, K. Maeda, A. Thomas, K. Takanabe, G. Xin, J. M. Carlsson, K. Domen and M. Antonietti, *Nat. Mater.*, 2009, **8**, 76–80.
52 P. Makuła, M. Pacia and W. Macyk, *J. Phys. Chem. Lett.*, 2018, **9**, 6814–6817.
53 F. Dong, Z. Zhao, T. Xiong, Z. Ni, W. Zhang, Y. Sun and W.-K. Ho, *ACS Appl. Mater. Interfaces*, 2013, **5**, 11392–11401.
54 L. Cheng, F. Chen, Z. Zhu, Y. Tang, K.-K. Shu and W. Shi, *Mater. Chem. Phys.*, 2022, **275**, 125192.
55 Q. He, M. Worku, L. Xu, C. Zhou, S. Lteif, J. B. Schlenoff and B. Ma, *J. Mater. Chem. A*, 2020, **8**, 2039–2046.
56 K. Das, S. N. Sharma, M. Kumar and S. K. De, *J. Phys. Chem. C*, 2009, **113**, 14783–14792.
57 B. Roose, S. Pathak and U. Steiner, *Chem. Soc. Rev.*, 2015, **44**, 8326–8349.
58 L. Wu, Y. Zhang, X. Li and C. Cen, *Phys. Chem. Chem. Phys.*, 2014, **16**, 15339.
59 Y.-F. Xu, M.-Z. Yang, B.-X. Chen, X.-D. Wang, H.-Y. Chen, D.-B. Kuang and C.-Y. Su, *J. Am. Chem. Soc.*, 2017, **139**, 5660–5663.
60 R. Das, S. Sarkar, R. Kumar, S. D. Ramarao, A. Cherevotan, M. Jasil, C. P. Vinod, A. K. Singh and S. C. Peter, *ACS Catal.*, 2022, **12**, 687–697.
61 K. Zhang, W. Kim, M. Ma, X. Shi and J. H. Park, *J. Mater. Chem. A*, 2015, **3**, 4803–4810.
62 S. Hoang, S. Guo, N. T. Hahn, A. J. Bard and C. B. Mullins, *Nano Lett.*, 2012, **12**, 26–32.
63 X. Zhao, Y. Fan, W. Zhang, X. Zhang, D. Han, L. Niu and A. Ivaska, *ACS Catal.*, 2020, **10**, 6367–6376.

64 J. Liu, J. Zhang, D. Wang, D. Li, J. Ke, S. Wang, S. Liu, H. Xiao and R. Wang, *ACS Sustainable Chem. Eng.*, 2019, **7**, 12428–12438.
65 R. Pandiyan, N. Delegan, A. Dirany, P. Drogui and M. A. El Khakani, *J. Phys. Chem. C*, 2016, **120**, 631–638.
66 I. Shown, H.-C. Hsu, Y.-C. Chang, C.-H. Lin, P. K. Roy, A. Ganguly, C.-H. Wang, J.-K. Chang, C.-I. Wu, L.-C. Chen and K.-H. Chen, *Nano Lett.*, 2014, **14**, 6097–6103.
67 R. Beranek, *Adv. Phys. Chem.*, 2011, **2011**, 1–20.
68 H. Fei, W. Leng, X. Li, X. Cheng, Y. Xu, J. Zhang and C. Cao, *Environ. Sci. Technol.*, 2011, **45**, 4532–4539.
69 R. Ghalta, A. Chauhan and R. Srivastava, *ACS Appl. Nano Mater.*, 2024, **7**, 1462–1476.
70 S. Raja, R. Ramesh Babu, S. Chandra Mohan, K. Jothivenkatachalam and K. Ramamurthi, *Appl. Surf. Sci.*, 2019, **497**, 143737.
71 X. Wang, X. Zheng, H. Han, Y. Fan, S. Zhang, S. Meng and S. Chen, *J. Solid State Chem.*, 2020, **289**, 121495.
72 L. Wang, M. I. Nathan, T.-H. Lim, M. A. Khan and Q. Chen, *Appl. Phys. Lett.*, 1996, **68**, 1267–1269.
73 P. D. Kouris, D. J. G. P. van Osch, G. J. W. Cremers, M. D. Boot and E. J. M. Hensen, *Sustainable Energy Fuels*, 2020, **4**, 6212–6226.
74 J. Yu, W. Wang, B. Cheng and B.-L. Su, *J. Phys. Chem. C*, 2009, **113**, 6743–6750.
75 S. Arumugam, T. Bavani, M. Selvaraj, B. M. Al-Shehri, M. Preeyanghaa, S. Jung, J. Theerthagiri, B. Neppolian, S. Murugesan, J. Madhavan and M. Y. Choi, *Chemosphere*, 2023, **313**, 137552.
76 E.-P. Bao, R. Dong, S. Zhang, H. Li, W. Zhang, J. Zou and Q. Xu, *Catal. Lett.*, 2021, **151**, 3437–3450.